

The Raman effect in femto- and attosecond physics

A M Zheltikov

DOI: 10.3367/UFNe.0181.201101c.0033

Contents

1. Introduction	29
2. Nonlinear-optical response and nonlinear-optical susceptibility	30
3. The quantum picture: Raman scattering as a tool for attosecond spectrochronography	31
4. Phase matching	32
5. Evolution of ultrashort optical pulses in a Raman-active medium	32
6. Molecular light modulators and controlled optical nonlinearity of molecular gases	34
7. The Raman effect and soliton frequency shift	37
8. Soliton fiber sources of extremely short electromagnetic pulses	38
9. Molecular modulators and the synthesis of ultrashort field waveforms	41
10. Fiber-optic synthesizers of ultrashort light pulses	42
11. Synthesizers of tailored sequences of ultrashort light pulses for single-beam coherent anti-Stokes Raman scattering microspectroscopy	42
12. Coherent Raman scattering of ultrashort light pulses by optical phonons	45
13. Optical detection of ultrafast physical processes on the attosecond time scale	48
14. Conclusion	50
References	50

Abstract. The interaction of ultrashort light pulses with matter is accompanied by a variety of new phenomena involving Raman scattering due to vibrational and rotational modes of molecules, electronic states of atoms and ions, and phonons in solids. These effects offer unique opportunities for an all-optical detection of ultrafast processes on the femto- and attosecond time scales, efficient spectral and temporal transformation of ultrashort field waveforms, and the highly sensitive microscopy of physical, chemical, and biological objects.

1. Introduction

The discovery of Raman scattering had a tremendous impact on the natural sciences. Observation of this effect was viewed as one of the most convincing proofs of the validity of quantum theory. The Raman effect provides a powerful tool for optical spectroscopy. Over the past eight decades, spectroscopic techniques based on Raman scattering have been successfully used for the identification of the composition

and spatial structure of physical, chemical, and biological objects. Exactly 80 years ago, only two years after the publication of the results of pioneering experiments on the Raman effect by Mandelstam, Landsberg, Raman, and Krishnan [1–5], one of the authors of this great discovery (C V Raman) was awarded the Nobel Prize in Physics 1930. The history of the discovery of the Raman effect has been the subject of extensive, illuminating literature [6–8].

With the advent of lasers, stimulated [9, 10] and coherent [11, 12] regimes of Raman scattering became feasible. Stimulated Raman scattering (SRS) has been widely used since then for the creation of efficient frequency converters [12, 13] and compact fiber lasers [14]. This phenomenon can provide a selective excitation of quantum states in atomic and molecular systems [15, 16] and allows the efficient generation of broadband radiation and few-cycle light pulses [17–19].

Spectroscopic methods based on coherent Raman scattering, including coherent anti-Stokes Raman scattering (CARS) [11, 12, 20, 21], have found extensive applications in studies of the structure of molecules, intermolecular interactions, chemical reactions, and energy transfer and relaxation in molecular systems, as well as the diagnostics of flames, ionized gases, and plasmas [20–25]. Coherent Raman scattering is at the heart of the recently developed novel method of chemically selective, marker-free, high-resolution microscopy, which is finding rapidly growing applications in the studies of structurally complex objects and biological systems [26, 27]. Much research is currently focused on identifying ways of applying CARS techniques for the standoff detection of potentially hazardous chemical and biological agents [28–31].

A M Zheltikov Physics Department, International Laser Center,
M V Lomonosov Moscow State University,
Vorob'evy gory, 119991 Moscow, Russian Federation
Tel. (7-495) 939 51 74
Fax (7-495) 939 31 13
E-mail: zheltikov@phys.msu.ru

Received 26 April 2010, revised 28 June 2010
Uspekhi Fizicheskikh Nauk **181** (1) 33 – 58 (2011)
DOI: 10.3367/UFNr.0181.201101c.0033
Translated by A M Zheltikov; edited by A Radzig

The wide adoption of quantum concepts in the early 20th century, including the quantum picture of light–matter interaction, has facilitated the correct understanding of experimental studies on Raman scattering as a new method of spectroscopy. One century later, a present generation of optical quantum sources enables implementation of novel regimes of Raman scattering involving extremely short light pulses. These regimes offer unique options for the investigation of ultrafast processes on the femto- and attosecond time scales, efficient spectral and temporal transformation of ultrashort field waveforms, and highly sensitive microscopy of physical, chemical, and biological objects. Here, we provide an overview of this rapidly growing field of optical physics. In what follows, we will consider the properties of Raman scattering by rotational and vibrational modes of molecular gases, optical phonons in solids, and the electronic states of atoms, ions, and molecules. We will review coherent and stimulated Raman scattering methods for the analysis of ultrafast processes in molecular and atomic systems on the femto- and attosecond time scales. We will also discuss Raman-effect-based techniques for the synthesis of extremely short light pulses, including few-cycle optical field waveforms and attosecond pulses.

2. Nonlinear-optical response and nonlinear-optical susceptibility

In standard spectroscopic schemes, Raman scattering gives rise to spectral sidebands shifted relative to the frequency of exciting radiation (pump) by the frequency Ω of the relevant Raman-active vibrational, rotational, librational, or excited optical phonon mode. Detection of Raman sidebands in the spectra of scattered radiation helps in identifying the chemical composition of gas mixtures and liquids, in understanding the kinetics of energy transfer in molecules and molecular aggregates, and in the study of the spatial structure of solids, including the analysis of quantum-size effects in nanostructured materials [13, 20–25, 32].

High-power laser radiation can amplify the Raman sidebands, giving rise to stimulated Raman scattering [10, 12]. Coherent excitation of Raman-active modes with a biharmonic pump or broadband optical field whose bandwidth $\Delta\omega$ exceeds Ω underlies the CARS technique for the local diagnostics of gases, plasmas, fluids, and solids. It also enables the coherent control of quantum processes in atomic and molecular systems [13, 20–25]. The Raman scattering of ultrashort light pulses is responsible for the emergence of new phenomena allowing a high-efficiency frequency transformation of ultrashort optical pulses and enabling a synthesis of few-cycle field waveforms [17, 18, 33–36]. Raman scattering can also give rise to a continuous downshift of the carrier frequency of an ultrashort light pulse, as part of its propagation dynamics in a nonlinear medium [14, 37–39].

To identify the general tendencies in the evolution of an ultrashort light pulse related to the nonlinear Raman effect, we consider the properties of the third-order nonlinear polarization induced by a light field in a medium:

$$P_{\text{nl}}(t) = \int_0^\infty \int_0^\infty \int_0^\infty \chi^{(3)}(t_1, t_2, t_3) E_1(t-t_1) E_2(t-t_2) \times E_3(t-t_3) dt_1 dt_2 dt_3. \quad (1)$$

Here, $E_{1,2,3}(\eta)$ are the light fields which generally have different carrier frequencies ω_1 , ω_2 , and ω_3 , temporal

envelopes, propagation directions, initial phases, and polarization states; $\chi^{(3)}(t_1, t_2, t_3)$ is the third-order nonlinear-optical response of the medium, which is related to the third-order nonlinear-optical susceptibility $\chi^{(3)}(\omega_1, \omega_2, \omega_3)$ through a Fourier transform:

$$\chi^{(3)}(\omega_1, \omega_2, \omega_3) \propto \int_0^\infty \int_0^\infty \int_0^\infty \chi^{(3)}(t_1, t_2, t_3) \times \exp [i(\omega_1 t_1 + \omega_2 t_2 + \omega_3 t_3)] dt_1 dt_2 dt_3. \quad (2)$$

Because of the high mobility of electrons, the inertia of the electronic part of the nonlinear-optical response can manifest itself only in very special regimes of interaction of ultrashort light pulses with matter, e.g., in the regime of multiphoton absorption. In the transparency range, the electronic nonlinearity can be usually treated as noninertial, with the electronic part of the nonlinear polarization instantaneously following the driving field:

$$\chi_{\text{K}}^{(3)}(t_1, t_2, t_3) = \chi_0 \delta(t_1) \delta(t_2) \delta(t_3), \quad (3)$$

$$P_{\text{nl}}(t) = \chi_{\text{K}} E_1(t) E_2(t) E_3(t). \quad (4)$$

In the spectral representation, the approximation specified by Eqn (3) corresponds to a purely nonresonant, nondispersive (i.e., frequency-independent) nonlinear susceptibility

$$\chi_{\text{K}}^{(3)}(\omega_1, \omega_2, \omega_3) \propto \chi_{\text{K}}. \quad (5)$$

Nonlinearity of this type is often referred to as Kerr nonlinearity.

Raman scattering effects accompany the interaction of light with particles or quasiparticles (atoms, molecules, molecular aggregates, phonons) whose nonlinear-optical response is much more inertial than the electronic optical nonlinearity. When the frequencies ω_1 , ω_2 , and ω_3 of optical fields involved in a nonlinear-optical process lie far away from one-photon non-Raman multiphoton resonances of a quantum system, the nonlinear-optical process giving rise to the anti-Stokes signal at the frequency $\omega_a = \omega_1 - \omega_2 + \omega_3$ with a Raman type resonance $\omega_1 - \omega_2 \approx \Omega$ (Fig. 1) is governed by the following cubic susceptibility:

$$\chi_{\text{R}}^{(3)}(t_1, t_2, t_3) = \chi_{\text{R}}(t_1) \delta(t_1 - t_2) \delta(t_3). \quad (6)$$

Substituting Eqn (6) into Eqn (1) and integrating over t_1 and t_3 , we derive the following expression for the nonlinear polarization:

$$P_{\text{nl}}(t) = E_3(t) \int_0^\infty \chi_{\text{R}}(t_1) E_1(t-t_1) E_2(t-t_1) dt_1. \quad (7)$$

The Fourier transform of formula (6) gives a nonlinear-optical susceptibility depending only on the frequency difference $\omega_1 - \omega_2$:

$$\begin{aligned} \chi_{\text{R}}^{(3)}(\omega_1, -\omega_2, \omega_3) &\propto \int_0^\infty \int_0^\infty \int_0^\infty \chi_{\text{R}}^{(3)}(t_1, t_2, t_3) \\ &\times \exp [i(\omega_1 t_1 - \omega_2 t_2 + \omega_3 t_3)] dt_1 dt_2 dt_3 \\ &= \int_0^\infty \chi_{\text{R}}(t_1) \exp [i(\omega_1 - \omega_2) t_1] dt_1 \equiv \chi_{\text{R}}(\omega_1 - \omega_2). \end{aligned} \quad (8)$$

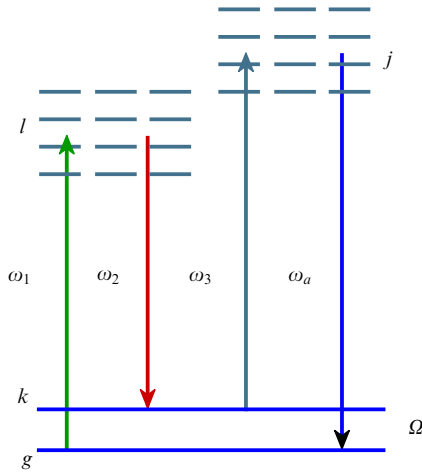


Figure 1. Diagram of the four-photon process involving nonlinear Raman scattering. The light fields with frequencies ω_1 (pump) and ω_2 (Stokes field) resonantly drive the Raman-active mode with the frequency Ω related to the $g \rightarrow k$ quantum transition. The probe field with the frequency ω_3 is scattered off the coherence induced by the pump and Stokes fields. The anti-Stokes signal with the frequency $\omega_a = \omega_1 - \omega_2 + \omega_3$ generated as a result of this nonlinear-optical process can provide spectroscopic information about the system, enable time-resolved studies of its dynamics, and allow a high-resolution chemically selective analysis of the spatial structure of an object.

The spectrum of the nonlinear susceptibility $\chi_R(\omega_1 - \omega_2)$ and its quantitative parameters (including the linewidth and the response time) are defined by the specific form of $\chi_R(t_1)$. In particular, $\chi_R(t_1)$ preset in the form of a damped harmonic oscillator corresponds to a Raman resonance with a Lorentzian line shape.

Physically, approximation (6) implies that the nonresonant optical response of the system can be considered instantaneous on the time scale defined by the pulse widths of the optical fields and the response time of the resonant part of nonlinear-optical susceptibility. In accordance with the uncertainty principle, the ratio between the response times of the resonant and nonresonant nonlinear-optical responses depends on the detuning of optical frequencies from the frequencies of quantum states (see Fig. 1). For the majority of Raman-active materials, this ratio may vary from two–three up to six–eight orders of magnitude. Delaying an ultrashort probe pulse by a time $\tau_d \sim 10$ fs is typically sufficient to substantially (by several orders of magnitude) suppress the contribution from the nonresonant part of medium polarization to the coherent Raman signal [22].

Formulas (3)–(5) introduce standard approximations conventionally used to describe transformations of optical pulses due to the Kerr effect. Off the edges of the transparency range (i.e., far from the UV absorption lines of atomic gases and the band gap of dielectric materials), these approximations provide an adequate description of Kerr-effect-induced nonlinear-optical processes, even for pulse widths close to the optical field cycle T_0 . However, for narrow-gap semiconductors, such as silicon, or strongly excited gas media, the approximations given by Eqns (3)–(5) may fail for pulse widths approaching T_0 . For such materials, the characteristic response time of Kerr nonlinearity is controlled by the frequency detuning of optical pulses from the edge of the transparency range [40].

3. The quantum picture: Raman scattering as a tool for attosecond spectrochronography

Representation of the nonlinear-optical response in the form of a product of delta functions in formulas (3) and (6) is, of course, a mathematical idealization. For the nonlinear Raman effect, such a model, as can be seen from expression (8), leads to a nonlinear-optical susceptibility that depends only on the frequency difference $\omega_1 - \omega_2$ and does not depend on any of the individual frequencies ω_1 , ω_2 , or ω_3 . The limitations of such an approximation and the physical meaning of the dependence of the nonlinear susceptibility $\chi_R^{(3)}$ on the frequencies ω_1 , ω_2 , and ω_3 become clear in the framework of the quantum theory of Raman scattering, which treats the coherent Raman effect as a result of the interaction of optical fields with eigenstates of a quantum system (see Fig. 1). The quantum model leads to the following expression [10, 12] for the third-order nonlinear-optical susceptibility corresponding to coherent Raman scattering through a transition between quantum states with energies $E_k = \hbar\omega_k$ and $E_g = \hbar\omega_g$ (see Fig. 1), so that $\omega_k - \omega_g = \Omega \approx \omega_1 - \omega_2$:

$$\chi^{(3)}(\omega_a = \omega_1 - \omega_2 + \omega_3) \propto \sum_{jl} \frac{\mu_{gj} \mu_{jk} \mu_{kl} \mu_{gl}}{(\omega_{jg} - \omega_a)(\omega_{kg} - (\omega_1 - \omega_2))(\omega_{lg} - \omega_1)}. \quad (9)$$

Here, μ_{gj} , μ_{jk} , μ_{kl} , and μ_{gl} are the matrix elements of the dipole moments for the $g \rightarrow j$, $j \rightarrow k$, $k \rightarrow l$, and $l \rightarrow g$ transitions, respectively; ω_{jg} and ω_{lg} are the frequencies of the $g \rightarrow j$ and $l \rightarrow g$ transitions, and $\omega_{kg} = \Omega$ is the frequency of the $g \rightarrow k$ Raman transition (see Fig. 1).

For coherent Raman scattering of ultrashort (i.e., broadband) light pulses under review, it is instructive to use Eqns (7)–(9) and represent the nonlinear polarization induced in the medium by optical fields as [41]

$$P_{nl}(\omega_a) \propto \int_0^\infty E_1(\omega') d\omega' \times \int_0^\infty \frac{E_2^*(\omega' - \omega'') E_3(\omega_a - \omega'')}{(\Omega - \omega'') + i\Gamma} d\omega'', \quad (10)$$

where $E_{1,2,3}(\omega)$ are the spectra of the optical fields, and Γ is the linewidth of the Raman-active transition. Expression (10) provides an accurate description of coherent Raman spectra in the regime of ultrashort pulses, including the Raman scattering of pulses with complicated and rapidly varying phase profiles [13, 41].

Expression (9) clearly demonstrate the dependence of the nonlinear Raman susceptibility $\chi_R^{(3)}$ on the frequency detunings of optical fields from the frequencies of quantum states. In accordance with the uncertainty principle, $\Delta E \Delta t \geq \hbar$, the frequency detunings $\Delta\omega_j = \omega_{jg} - \omega_a$ and $\Delta\omega_l = \omega_{lg} - \omega_1$, appearing in expression (9), define the upper-bound limits $\Delta\tau_j \leq (\Delta\omega_j)^{-1}$ and $\Delta\tau_l \leq (\Delta\omega_l)^{-1}$ for excitation times of the energy states contributing to coherent Raman scattering as virtual levels (see Fig. 1). Since the time intervals $\Delta\tau_j$ and $\Delta\tau_l$ are small, Raman light scattering can be employed to retrieve the information on the ultrafast evolution of the wave function of an excited quantum system. Indeed, methods of Raman X-ray scattering, implemented with the use of synchrotron sources, provide information on the wave-packet dynamics of electronically excited molecular states

with attosecond time resolution [42]. For a broad class of organic dyes with a characteristic red edge of absorption band near 350 nm, excited by infrared (IR) radiation of commonly used femtosecond lasers (at 800 nm in the case of a Ti:sapphire laser, and 1.25 μm in the case of a Cr:forsterite laser), the response times $\Delta\tau_j$ and $\Delta\tau_l$ fall within the range from 250 to 300 as ($1 \text{ as} = 10^{-18} \text{ s}$). When the frequencies of optical fields are chosen close to the frequencies of the relevant energy states, enhancement of coherent Raman scattering, as can be seen from Eqn (9), is achieved at the expense of increased excitation times of the quantum states involved in the Raman scattering process (virtual states in Fig. 1) and stronger inertia of the Raman response of the system [40].

4. Phase matching

The efficiency of energy transfer from laser fields to the signal of coherent Raman light scattering is limited by phase mismatch between the wave of nonlinear polarization P_{nl} and the field generated through coherent Raman scattering [10, 12]. For the process responsible for generating an anti-Stokes signal at the central frequency $\omega_a = \omega_1 - \omega_2 + \omega_3$ in optical fields with central frequencies ω_1 , ω_2 , and ω_3 , the phase mismatch controlling the efficiency of coherent Raman scattering is written out as

$$\Delta\varphi = \varphi_a - \varphi_p = \varphi_a - \varphi_1 + \varphi_2 - \varphi_3,$$

where φ_a is the phase of the anti-Stokes field, φ_p is the phase of the nonlinear polarization wave, and $\varphi_{1,2,3}$ are the phases of the laser fields with the frequencies $\omega_{1,2,3}$.

The phase mismatch $\Delta\varphi$ can be represented as a sum $\Delta\varphi = \Delta\varphi_d + \Delta\varphi_g + \Delta\varphi_{\text{nl}}$, where $\Delta\varphi_d$ is the phase mismatch due to matter dispersion (frequency dependence of the refractive index), and $\Delta\varphi_g$ and $\Delta\varphi_{\text{nl}}$ include geometric and nonlinear (intensity-dependent) phase shifts for the fields involved in the nonlinear-optical process. For plane waves, the phase mismatch induced by the dispersion of the medium is given by

$$\Delta\varphi_d = c^{-1}(\omega_a n_a - \omega_1 n_1 + \omega_2 n_2 - \omega_3 n_3),$$

where n_a and $n_{1,2,3}$ are the refractive indices of the medium at the frequencies ω_a and $\omega_{1,2,3}$.

The maximum coupling between the optical fields involved in the nonlinear-optical process and, consequently, the highest efficiency of coherent Raman signal generation are achieved in the phase-matching regime, when $\Delta\varphi = 0$. This phase-matching condition can be commonly satisfied [13] through an appropriate choice of a noncollinear beam geometry of the nonlinear-optical interaction or through the compensation for the material part of the phase mismatch $\Delta\varphi_d$ by the geometric phase $\Delta\varphi_g$. A broad class of guided-wave nonlinear-optical processes can be phase-matched by using dispersion of waveguide modes [14]. Dispersion profiles of these modes can be tailored through waveguide structure engineering [43]. With this approach, nonlinear-optical processes can be phase-matched within a broad range of frequencies, enabling highly efficient frequency conversion of ultrashort laser pulses [44, 45]. For certain dispersion profiles, the phase mismatch $\Delta\varphi_{\text{nl}}$ induced by the nonlinear phase shift can give rise to modulation instabilities of optical fields [14], allowing controlled transformations of the spectrum and temporal envelope of ultrashort light pulses [13].

5. Evolution of ultrashort optical pulses in a Raman-active medium

Analysis of the nonlinear phase shift is the key to understanding a broad class of nonlinear-optical processes involving ultrashort light pulses, including self- and cross-phase modulation, solitonic effects, and modulation instabilities. In nonlinear Raman scattering, analysis of a nonlinear phase shift becomes especially important when the bandwidths of optical fields become comparable to or larger than the frequencies of Raman-active modes.

An ultrashort optical pulse propagating in a medium with both Kerr and Raman optical nonlinearities [see Eqns (3) and (6)] experiences a nonlinear phase shift [14, 46]:

$$\varphi(\eta, z) = -k_0 n_2 z \int_{-\infty}^{\eta} I(\xi) R(\eta - \xi) d\xi, \quad (11)$$

where $k_0 = 2\pi/\lambda$, λ is the central wavelength of the light pulse, $n_2 = (2\pi/n_0)^2 \chi^{(3)}(\omega, -\omega, \omega)$ is the nonlinear refractive index of the medium, n_0 is the refractive index of the medium in the absence of the light field, z is the propagation coordinate, η is the retarded time (i.e., the time in the frame of reference moving with the group velocity of the light pulse), $I(\eta)$ is the temporal profile of the field intensity, and

$$R(\theta) = (1 - f_R) \delta(\theta) + f_R H(\theta) \quad (12)$$

is the nonlinear-optical response of the medium [47, 48]. The delta-function term in expression (12) describes the instantaneous Kerr type nonlinearity [cf. expression (3)]. The retarded part of the nonlinear-optical response is described by the function $H(\theta)$, which is related to the nonlinear-optical susceptibility $\chi_R(\omega_1 - \omega_2)$, defined by formula (6), by the expression [47, 48]

$$H(\theta) \propto \int_{-\infty}^{\infty} \chi_R(\omega) \exp(-i\omega\theta) d\omega.$$

The weighting factor f_R is introduced to quantify the fraction of retarded nonlinearity in the overall nonlinear-optical response of the medium.

Substituting Eqn (12) into Eqn (11), we find

$$\varphi(\eta, z) = \varphi_K(\eta, z) + \varphi_R(\eta, z), \quad (13)$$

where

$$\varphi_K(\eta, z) = -k_0 n_2 z (1 - f_R) I(\eta), \quad (14)$$

$$\varphi_R(\eta, z) = -k_0 n_2 z f_R \int_{-\infty}^{\eta} I(\xi) H(\eta - \xi) d\xi. \quad (15)$$

Formula (14) gives a standard expression for the nonlinear phase shift related to the instantaneous Kerr type optical nonlinearity. The phase shift φ_K scales linearly with the nonlinear refractive index n_2 , the interaction length z , and the peak intensity I_0 , with $I(\eta) = I_0 \psi(\eta)$, and $\psi(\eta)$ being the unity-normalized temporal intensity profile. Around the peak of a light pulse with an arbitrary temporal envelope, the Taylor series expansion of the field intensity profile yields

$$\psi(\eta) \approx 1 + \frac{1}{2} \frac{\partial^2 \psi}{\partial \eta^2} \Big|_{\eta=0} \eta^2. \quad (16)$$

For this section of the pulse, the Kerr effect induces a quadratic phase shift (a linear chirp), with the deviation $\delta\omega(t) = \omega(t) - \omega_0$ of the instantaneous frequency $\omega(t)$ from the central frequency ω_0 given by

$$\begin{aligned} \delta\omega_{\text{K}}(t) &= \frac{\partial\varphi_{\text{K}}}{\partial t} = -k_0 n_2 z I_0 (1 - f_{\text{R}}) \frac{\partial\psi(\eta)}{\partial\eta} \\ &\approx k_0 n_2 z I_0 (1 - f_{\text{R}}) \left. \frac{\partial^2\psi}{\partial\eta^2} \right|_{\eta=0} \eta. \end{aligned} \quad (17)$$

In a particular case of a Gaussian pulse

$$\psi(\eta) = \exp\left(-\frac{\eta^2}{\tau_{\text{p}}^2}\right), \quad (18)$$

the Kerr-effect-induced phase shift (14) takes the form

$$\varphi_{\text{K}}(\eta, z) = -k_0 n_2 z (1 - f_{\text{R}}) I_0 \exp\left(-\frac{\eta^2}{\tau_{\text{p}}^2}\right). \quad (19)$$

Around the peak of the light pulse, $\eta/\tau_{\text{p}} \ll 1$, where $\psi(\eta) \approx 1 - \eta^2/\tau_{\text{p}}^2$, we have

$$\delta\omega_{\text{K}}(t) \approx 2k_0 n_2 z I_0 (1 - f_{\text{R}}) \frac{\eta}{\tau_{\text{p}}^2}. \quad (20)$$

Evaluation of the phase shift induced by the inertial nonlinearity requires knowledge of the response function $H(\xi)$. In a widely used model of nonlinear Raman scattering, the retarded part of optical nonlinearity is described as a damped oscillator:

$$H(\theta) = \frac{\tau_1^2 + \tau_2^2}{\tau_1 \tau_2} \sin\left(\frac{\theta}{\tau_1}\right) \exp\left(-\frac{\theta}{\tau_2}\right) \Theta(t), \quad (21)$$

where $\tau_1 = \Omega_{\text{R}}^{-1}$, τ_2 is the decay time of the Raman-active mode, and $\Theta(t)$ is the Heaviside step function. The damped-oscillator model (21) with different values of τ_1 and τ_2 parameters provides a reasonable approximation for the description of different types of Raman-active systems, like the molecular gases [49–51] (including atmospheric air), semiconductor solids [52], and fused silica utilized in optical fibers [14, 47, 48]. Below, we will discuss in greater detail the physical content and limitations of the damped-oscillator model in the case of molecular gases and solids (see Section 5).

In the case of a Gaussian pulse, the retarded nonlinearity with the response function given by Eqn (21) gives rise to a nonlinear phase shift [46]

$$\begin{aligned} \varphi_{\text{R}}(\eta, z) &= -k_0 n_2 z f_{\text{R}} i I_0 \frac{\sqrt{\pi}}{4} \frac{\tau_{\text{p}}(\tau_1^2 + \tau_2^2)}{\tau_1 \tau_2} \\ &\times \left\{ \exp\left[\frac{\tau_{\text{p}}^2}{4} \left(\frac{1}{\tau_2} - \frac{2\eta}{\tau_{\text{p}}^2} + \frac{i}{\tau_1}\right)^2\right] \operatorname{erfc}\left[\frac{\tau_{\text{p}}}{2} \left(\frac{1}{\tau_2} - \frac{2\eta}{\tau_{\text{p}}^2} + \frac{i}{\tau_1}\right)\right] \right. \\ &\left. - \exp\left[\frac{\tau_{\text{p}}^2}{4} \left(\frac{1}{\tau_2} - \frac{2\eta}{\tau_{\text{p}}^2} - \frac{i}{\tau_1}\right)^2\right] \operatorname{erfc}\left[\frac{\tau_{\text{p}}}{2} \left(\frac{1}{\tau_2} - \frac{2\eta}{\tau_{\text{p}}^2} - \frac{i}{\tau_1}\right)\right] \right\}, \end{aligned} \quad (22)$$

where

$$\operatorname{erfc}\theta = 1 - 2\pi^{-1/2} \int_0^\theta \exp(-\xi^2) d\xi.$$

For a weakly inertial response, with $\tau_1, \tau_2 \ll \tau_{\text{p}}$, an asymptotical expression $\operatorname{erfc}\zeta \approx \zeta^{-1} \pi^{-1/2} \exp(-\zeta^2)$, which is valid for large values of the argument, brings Eqn (22) to the

form

$$\varphi_{\text{R}}(\eta, z) \approx -k_0 n_2 z f_{\text{R}} I_0 \exp\left(-\frac{\eta^2}{\tau_{\text{p}}^2}\right) \left(1 + 2\mu \frac{\eta}{\tau_{\text{p}}}\right), \quad (23)$$

where a small parameter $\mu = \tau_{\text{p}}^{-1} \tau_2^{-1} (\tau_1^{-2} + \tau_2^{-2})^{-1}$ has been introduced.

As can be seen from expressions (19) and (23), a weak inertia of the nonlinear-optical response in a linear approximation in a small parameter μ is included in the nonlinear phase shift through a factor $1 + 2\mu\eta/\tau_{\text{p}}$. Around the peak of the pulse, $\eta/\tau_{\text{p}} \ll 1$, where $\psi(\eta) \approx 1 - \eta^2/\tau_{\text{p}}^2$, this factor gives rise to linear ($\propto \mu\eta/\tau_{\text{p}}$) and cubic ($\propto \mu\eta^3/\tau_{\text{p}}^3$) phase terms, in addition to the quadratic phase $\propto \eta^2/\tau_{\text{p}}^2$, which also appears in the expression for the Kerr-effect-related nonlinear phase. The related frequency deviation around the peak of the pulse takes on the form

$$\delta\omega_{\text{R}}(t) \approx 2k_0 n_2 z I_0 f_{\text{R}} \left[\frac{\eta}{\tau_{\text{p}}^2} - \frac{\mu}{\tau_{\text{p}}} \left(1 - 3 \frac{\eta^2}{\tau_{\text{p}}^2}\right) \right]. \quad (24)$$

In addition to the linear chirp represented by the $\propto \eta/\tau_{\text{p}}^2$ term, formula (24) also includes small corrections, implying a uniform frequency downshift $\propto -\mu/\tau_{\text{p}}$ and a quadratic chirp $\propto (\mu/\tau_{\text{p}})(\eta/\tau_{\text{p}})^2$. Continuous red shifting of ultrashort pulses, induced by retarded optical nonlinearity, was extensively studied earlier for the regime of anomalous dispersion, where this effect is usually referred to as the optical soliton self-frequency shift. In the solitonic regime, where the peak power of a soliton scales as $P \propto \tau_{\text{s}}^{-2}$ with the soliton pulse width, the soliton frequency shift rate $\partial|\Delta f|/\partial z$ (Δf is the soliton frequency shift) has been shown to scale as τ_{s}^{-4} [53], as long as the Raman gain profile can be approximated with a linear function of radiation frequency.

For nonsolitonic light pulses, i.e., assuming no balance between dispersion and nonlinearity, the peak power scales simply as τ_{p}^{-1} with the pulse width, leading to a τ_{p}^{-3} scaling law for the rate of frequency downshift (see also paper [54]). Both the τ_{s}^{-4} and τ_{p}^{-3} scaling laws for the rate of the frequency downshift of a light pulse are readily recovered by taking the derivative $\partial(|\delta\omega_{\text{R}1,2}|)/\partial z$ of the frequency shift defined by expression (24) and making a substitution $I_0 = P/S \propto \tau_{\text{s}}^{-2}$ for the solitonic regime, and $I_0 = P/S \propto \tau_{\text{p}}^{-1}$ for the nonsolitonic pulses (S being the effective light beam area).

In the opposite limiting case of extremely short light pulses, $\tau_{\text{p}} \ll \tau_1, \tau_2$, and strongly inertial optical nonlinearity, integration in formula (14) with the response function $H(\theta)$ defined by expression (21) yields [46]

$$\varphi_{\text{R}}(\eta, z) \approx -k_0 n_2 z f_{\text{R}} I_0 \frac{\sqrt{\pi}}{2} \varepsilon \operatorname{erfc}\left(-\frac{\eta}{\tau_{\text{p}}}\right), \quad (25)$$

where $\varepsilon = \tau_1 \mu^{-1} \tau_2^{-1} = \tau_{\text{p}} \tau_1 (\tau_1^{-2} + \tau_2^{-2})$ is a small parameter.

Around the peak of the light pulse, $\eta/\tau_{\text{p}} \ll 1$, a Taylor-series expansion

$$\operatorname{erfc}\zeta \approx 1 - 2\pi^{-1/2} \left(\zeta - \frac{\zeta^3}{3} + \frac{\zeta^5}{10} \right)$$

brings expression (25) to the form

$$\varphi_{\text{R}}(\eta, z) \approx -k_0 n_2 z f_{\text{R}} \varepsilon I_0 \left[\frac{\sqrt{\pi}}{2} + \frac{\eta}{\tau_{\text{p}}} - \frac{1}{3} \left(\frac{\eta}{\tau_{\text{p}}}\right)^3 + \frac{1}{10} \left(\frac{\eta}{\tau_{\text{p}}}\right)^5 \right]. \quad (26)$$

In this regime, the phase and frequency shifts induced by the inertial part of optical nonlinearity are intrinsically small because a light pulse in the regime considered is too short to efficiently couple an optical field to Raman-active modes. In what follows, we will consider specific features of interaction of ultrashort light pulses with Raman-active modes of different natures, including vibrations and rotations of molecules in a gas and optical phonons in solids.

6. Molecular light modulators and controlled optical nonlinearity of molecular gases

The Raman scattering of light by rotational and vibrational modes of molecules plays a significant role in the dynamics of ultrashort laser pulses propagating through a molecular gas. The bandwidth of sub-100-fs laser pulses, widely used in ultrafast optical experiments, is sufficient for the excitation of multiple rotational Raman modes. Phased excitation of molecular rotations gives rise to periodic recurrences in the modulation of the refractive index $\Delta n(\eta)$. A femtosecond probe pulse with a central wavelength λ , delayed in time with respect to the pump pulse inducing molecular rotations, will then acquire a phase shift

$$\varphi_{\text{nl}}(\eta) = \frac{2\pi}{\lambda} l \Delta n(\eta) \quad (27)$$

depending on the nonlinear-optical interaction length l , and will experience the corresponding frequency shift.

The Raman response of molecular rotations is usually described as a sum over molecular rotational transitions [55–58], mimicked by harmonic terms:

$$R(\theta) \propto \sum_J F_J \sin(-\omega_J \theta), \quad (28)$$

where J is the rotational quantum number, and

$$F_J = (\rho_{J+1} - \rho_J) \frac{Z_J(J+2)(J+1)}{2J+3}, \quad (29)$$

$$\rho_J = \exp \left[-\frac{chBJ(J+1)}{kT} \right] \times \left\{ \sum_J Z_J(2J+1) \exp \left[-\frac{chBJ(J+1)}{kT} \right] \right\}^{-1}, \quad (30)$$

where h is the Planck constant, c is the speed of light in vacuum, k is the Boltzmann constant, T is the gas temperature, B is the rotational constant, Z_J is a factor describing the quantum nuclear statistics, and

$$\omega_J = 4\pi Bc(2J+3) \quad (31)$$

are the frequencies of rotational transitions in the rigid-rotor approximation.

For molecular nitrogen (N_2), whose content in atmospheric air is about 80%, the constants appearing in Eqns (28)–(31) are specified as $B \approx 1.99 \text{ cm}^{-1}$, $Z_J = 1$ and 2, for odd and even J , respectively [58]. For molecular oxygen (O_2), comprising about 20% of atmospheric air, $B \approx 1.44 \text{ cm}^{-1}$, $Z_J = 1$ and 0 for odd and even J , respectively [58].

As can be seen from formulas (28)–(31), rotational Raman spectra are sensitive to the gas temperature. This property of Raman scattering in gases (including nonlinear versions of Raman scattering, such as CARS) is widely used

for the thermometry of gases, flames, and plasmas [20, 21]. As the gas temperature rises, population becomes redistributed over a larger number of rotational states, while the population differences controlling the intensities of rotational Raman transitions tend to decrease. As a result, an increase in temperature leads to the broadening of rotational Raman spectral branches and reduces their peak amplitudes.

In the time domain, series of rotational transitions observed in rotational Raman spectra translate into a sum of harmonically oscillating terms, each representing a rotational Raman transition with a frequency ω_J . The difference of adjacent transition frequencies, namely

$$\Delta\omega = \omega_{J+1} - \omega_J = 8\pi Bc, \quad (32)$$

is independent of J , and the time-domain Raman response displays rotational echo recurrences (Figs 2a–c) corresponding to a periodic phasing of molecular rotators, also known as revivals of rotational wave packets [59, 60]. The duration of each recurrence transient in the Raman response is determined by the scatter of molecular rotators in their frequencies—that is, by the width $\delta\omega$ of the rotational Raman spectrum, and is thus sensitive to the gas temperature (Figs 2a–c). Coherence relaxation of molecular rotations leads to an exponential decay of recurrences in the rotational Raman response with a characteristic decay time of 61 ps in the case of molecular nitrogen, and 68 ps for molecular oxygen.

Polarization properties of the retarded nonlinear-optical response of a Raman-active gas are controlled by the tensor properties of the relevant nonlinear-optical susceptibility. An isotropic medium is described by three independent tensor components χ_{ijkl} ($i, j, k, l = 1, 2, 3$) which can be chosen among the following four physically significant tensor elements [12, 61]:

$$\chi_{1111} \propto \frac{1}{3} G_1 + \frac{2}{3} G_2, \quad (33)$$

$$\chi_{1212} \propto \frac{1}{2} G_2 - \frac{1}{2} G_3, \quad (34)$$

$$\chi_{1221} \propto \frac{1}{2} G_2 + \frac{1}{2} G_3, \quad (35)$$

$$\chi_{1122} \propto \frac{1}{3} G_1 - \frac{1}{3} G_2, \quad (36)$$

where G_1 , G_2 , and G_3 are the autocorrelation functions of the isotropic, symmetric, and antisymmetric parts of molecular polarizability, respectively, which represent rotation-invariant molecular parameters. As can be seen from formulas (33)–(36), the nonlinear-optical susceptibility tensor components satisfy the relation $\chi_{1212} + \chi_{1221} + \chi_{1122} = \chi_{1111}$, which is typical of an isotropic medium. The polarization sensitivity of the nonlinear-optical response of a gas medium, governed by Eqns (33)–(36), enables control over the amplitude and phase of echo recurrences of the refractive index $\Delta n(\eta)$ by varying polarization states of the pump and probe fields.

Experiments on polarization and phase control of the retarded optical nonlinearity of the atmosphere were performed [62] with the use of a femtosecond laser system consisting of a mode-locked Ti:sapphire laser oscillator pumped by the second-harmonic output of a neodymium garnet laser, and a multipass amplifier. This femtosecond laser system delivered light pulses with a central wavelength

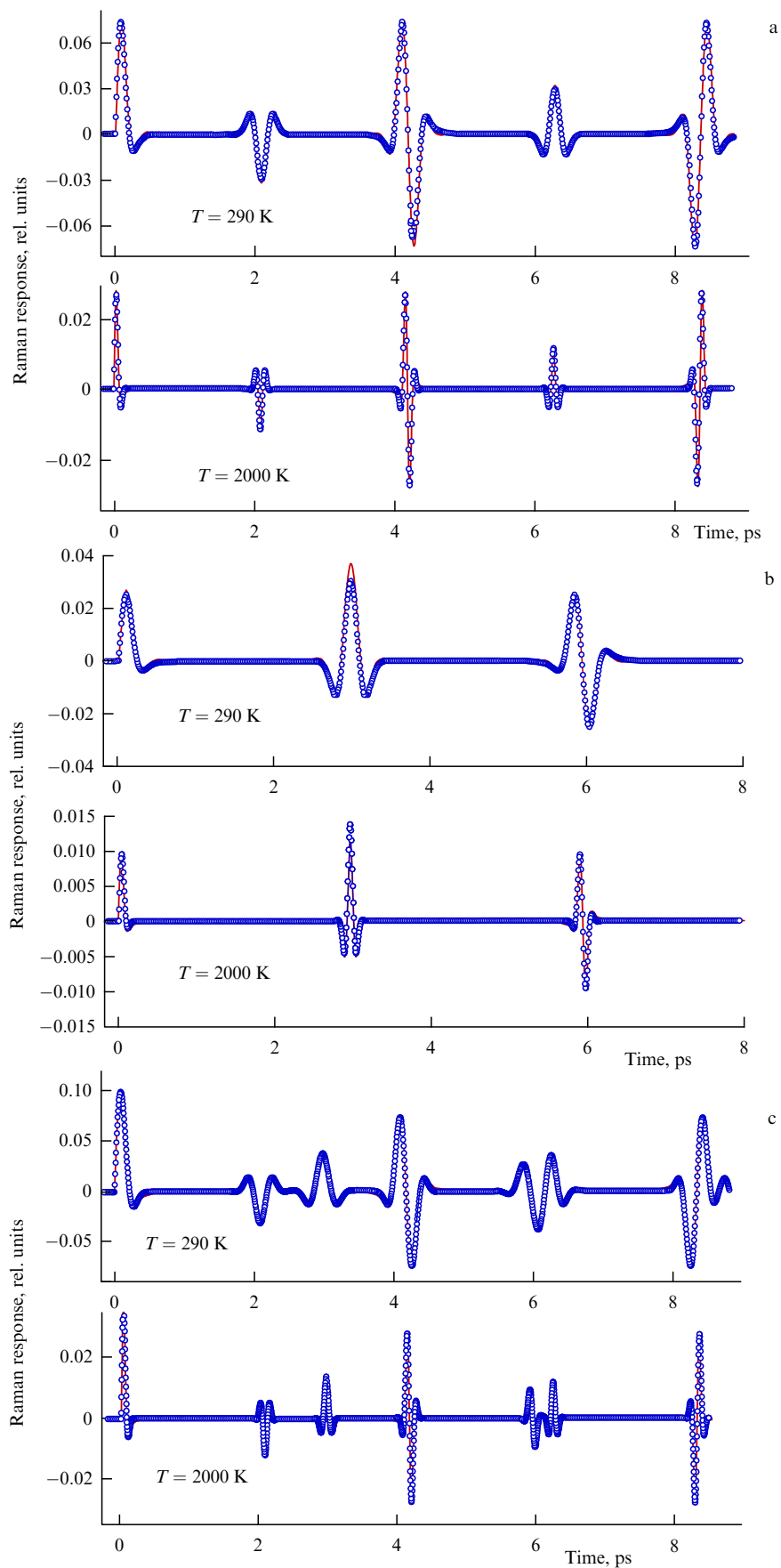


Figure 2. The Raman response of rotational modes of (a) molecular nitrogen, (b) molecular oxygen, and (c) atmospheric air (consisting of 80% molecular nitrogen and 20% molecular oxygen) calculated with the use of Eqns (26)–(29) (solid lines) and Eqn (31) (circles).

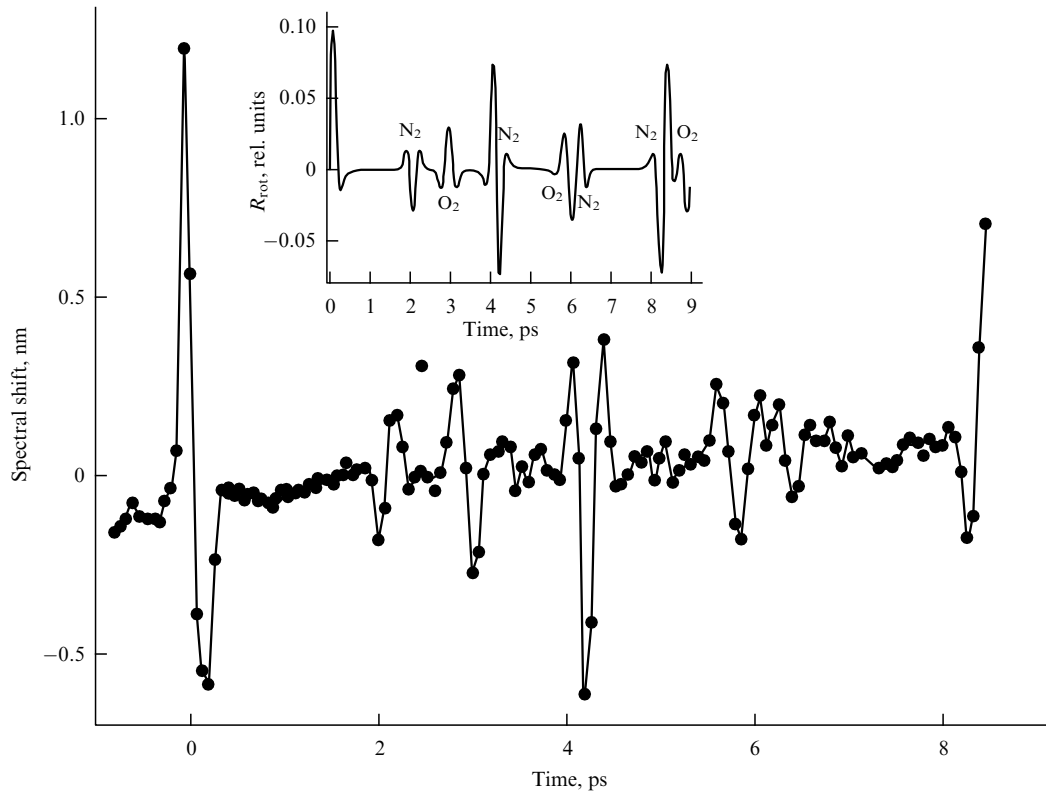


Figure 3. Central wavelength shift of the probe pulse as a function of the delay time between the probe and pump pulses. The pump pulse energy is 0.8 mJ. The pulse widths of the pump and probe pulses are 50 fs. The pump field is polarized parallel to the field polarization of the probe pulse. The inset shows the rotational part of the Raman function R_{rot} of atmospheric air calculated with the use of Eqns (26)–(29) at a gas temperature of 290 K. Also shown is the assignment of the echo revivals of the Raman function to the rotational modes of nitrogen and oxygen molecules.

of about 800 nm, a pulse width of 50 fs, and an energy of up to 1.5 mJ at a repetition rate of 50 Hz.

Figure 3 presents the central wavelength shift $\delta\lambda_p$ of a weak probe 50-fs laser pulse measured as a function of the delay time τ between the probe pulse and a single 50-fs, 0.8-mJ pump pulse [62]. The $\delta\lambda_p(\tau)$ dependence displays well-resolved echo recurrences related to excited rotations of oxygen and nitrogen molecules in atmospheric air. Due to the large decay times of rotational coherences (61 and 68 ps for N_2 and O_2 molecules, respectively, under normal conditions), periodic phasing of molecular rotations gives rise to extended sequences of echo recurrences, which show up in the $\lambda_p(\tau)$ chronogram. Importantly, the echo recurrences separated by time intervals $\delta t = (4Bc)^{-1}$ are opposite in phase, i.e., they have a π phase shift. This property of rotational echo recurrences helps distinguish temporal markers encoded in the neighboring recurrences. Because of the difference in the rotational constants of O_2 and N_2 molecules, on the other hand, the sequence of echo recurrences related to rotations of O_2 molecules is shifted in time with respect to the echo recurrences of N_2 rotations. Since temporal markers follow with different time intervals within each $\delta t = (4Bc)^{-1}$ cycle, different segments in echo-recurrence sequences can be easily distinguished from each other.

A variation in the angle θ between polarization vectors of the pump and probe fields noticeably modifies the waveform of echo recurrences. Specifically, oscillations in the phase of the probe field, induced by a pump field with parallel ($\theta = 0$) and orthogonal ($\theta = \pi/2$) polarizations, have different amplitudes and are opposite in phase. These properties of the nonlinear-optical response of the atmosphere can be

readily explained in terms of the tensor properties of its nonlinear-optical susceptibility. As is seen from formulas (33)–(36), when the polarization vectors of the pump and probe fields are parallel to each other, $\theta = 0$, the signal detected in the above-described experiment is controlled by the tensor component χ_{1111} . When the polarization of the pump field is perpendicular to the polarization of the probe field, $\theta = \pi/2$, the signal is determined by χ_{1122} . Thus, oscillations in the signal are related to the autocorrelation function of the symmetric part of molecular polarizability G_2 with both polarization arrangements. However, the term including G_2 in the expression for χ_{1122} is opposite in phase to and two times smaller than the G_2 -containing term of χ_{1111} . Echo recurrences measured with different polarizations of the pump and probe fields visualize this difference in tensor components χ_{ijkl} of the nonlinear-optical susceptibility of atmospheric air.

For the analysis of the time dependence of the birefringence induced in a gas medium by a high-power pump pulse, the polarization vector of a linearly polarized pump is set at an angle $\theta = \pi/4$ with respect to the polarization vector of the pump. A polarization analyzer is adjusted in such a way as to block the probe field in the absence of the pump beam. The detected signal in this experimental arrangement is at the level of detector noise. With the pump field turned on, echo recurrences related to rotations of nitrogen and oxygen molecules show up (see Fig. 3). The signal detected in this polarization geometry is controlled, in accordance with expressions (34) and (35), by the autocorrelation function of the symmetric part in the molecular polarizability, $\chi_{1212} + \chi_{1221} \propto G_1$. The birefringence read out by the probe pulse is

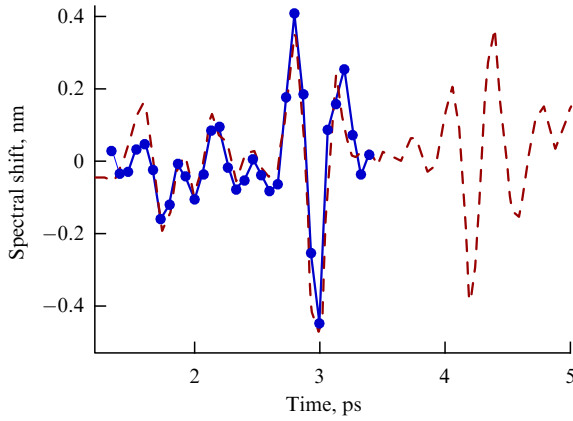


Figure 4. Shaping the temporal profile of the retarded nonlinear-optical response of atmospheric air with a pump field consisting of two femtosecond pulses. The central wavelength shift of a probe laser pulse measured as a function of the delay time between the pump and probe pulses with a pump field consisting of two 50-fs Ti:sapphire-laser pulses with an energy of 0.4 mJ each separated by a delay time $\delta \approx 1260$ fs. Filled circles connected with a solid line represent the experimental data. The dashed curve displays the $\delta\lambda_p(\tau) + \delta\lambda_p(\tau + \delta)$ function calculated from the experimental $\delta\lambda_p(\tau)$ dependence measured with a single-pulse pump.

determined by the pump intensity and delay time between the pump and probe light pulses. Thus, this polarization arrangement enables the gating of high-power ultrashort laser pulses, including those transmitted over large distances through the atmosphere. This approach can help synchronize high-power optical pulses separated by large distances and read out the information encoded in these pulses.

Pump fields consisting of sequences of ultrashort pulses can be employed to shape and tailor temporal profiles of refraction modulation $\Delta n(\eta)$. Figure 4 displays the wavelength shift of the probe field measured as a function of the delay time between the probe pulse and the second pump pulse in experiments where the pump field consisted of two 50-fs pulses with an energy of 0.4 mJ each [62]. The delay time between the pump pulses in these experiments was set equal to $\delta \approx 1260$ fs. To facilitate the understanding of these measurements, the dashed line in Fig. 4 shows the sum $\delta\lambda_p(\tau) + \delta\lambda_p(\tau + \delta)$, where $\delta\lambda_p(\tau)$ is the time-dependent central wavelength shift of the probe pulse, calculated using the experimental $\delta\lambda_p(\tau)$ dependence measured with a single-femtosecond-pulse pump (see Fig. 3). As can be seen from the results presented in Fig. 4, the first and second pump pulses give rise to virtually identical sequences of echo recurrences shifted with respect to each other by the delay time δ . Because of the decay of the rotational coherence with a decay time τ_r , the amplitudes of the respective echo recurrences in these sequences are slightly different. This difference is quantified in terms of a factor $\xi = \exp(-\delta/\tau_r) \approx 1 - \delta/\tau_r$. For a delay time $\delta \approx 1260$ fs, we have $\xi \approx 0.979$ and 0.981 for nitrogen ($\tau_r \approx 61$ ps) and oxygen ($\tau_r \approx 68$ ps) molecules, respectively. The temporal profile of $\Delta n(\eta)$ can be tailored by varying the delay time between the probe and pump pulses, enabling a pulse shaping of high-power ultrashort laser pulses transmitted over large distances through the atmosphere.

Experiments discussed in this section demonstrate the possibility of polarization and phase control of the retarded optical nonlinearity of atmospheric air related to rotations of nitrogen and oxygen molecules. These experiments implement amplitude and phase control of echo recurrences of the

refractive index of a gas medium by ultrashort laser pulses with variable intensities, polarizations, and waveforms [62]. Polarization sensitivity of the nonlinear-optical susceptibility controlling the Raman response of a medium is shown to enable gating of high-power ultrashort laser pulses, including pulses transmitted over large distances through the atmosphere. This approach can help synchronize high-power optical pulses separated by large distances and read out the information encoded in these pulses. Pump fields consisting of sequences of ultrashort pulses can be used to shape and tailor temporal profiles of refraction modulation in a gas medium. This approach suggests ways for controlled pulse [62, 63] and beam [64] shaping of high-power ultrafast field waveforms, including high-power ultrashort laser pulses transmitted over large distances through the atmosphere.

7. The Raman effect and soliton frequency shift

New physical effects related to the nonlinear Raman scattering of ultrashort pulses show up in the soliton regime. The inertia of optical nonlinearity, which is inherent in the Raman effect, can give rise to a continuous red shift of the carrier frequency of a soliton propagating through an optical fiber [14, 37, 38]. In the spectral domain, this phenomenon can be understood as stimulated Raman amplification of the low-frequency part of the soliton spectrum at the expense of depletion of its high-frequency wing. This effect, known as soliton self-frequency shift (SSFS), lies at the heart of a new generation of fiber-optic components for tunable wavelength conversion of ultrashort laser pulses [65].

Soliton self-frequency shift becomes possible due to the Raman scattering of light by optical phonons in fiber material. The Raman response of fused silica, the most common material in fiber fabrication, originates from several Raman-active vibrations of SiO_4 tetrahedra [66–68]. The most intense Raman-active mode, which shows up as the prominent peak centered around 440 cm^{-1} in the Raman gain spectrum of fused silica, corresponds to oscillations of the Si–O–Si dihedral angle of the tetrahedral unit cell of fused silica about its equilibrium value.

To analyze the dynamics of carrier shifting of an ultrashort soliton in a nonlinear medium with retarded nonlinearity, we apply the method proposed by Gordon [53]. This method involves a spectral transformation of the nonlinear Schrödinger equation (NSE)

$$-i \frac{\partial u}{\partial z} = \frac{1}{2} \frac{\partial^2 u}{\partial t^2} + |u|^2 u \quad (37)$$

for the pulse envelope u . The units of time (t_s) and length (z_s) in equation (37) are chosen in such a way that

$$\frac{t_s^2}{z_s} = \frac{\lambda^2 D}{2\pi c} = -\frac{\partial^2 \beta}{\partial \omega^2}, \quad (38)$$

$$P_s z_s = \frac{\lambda A_{\text{eff}}}{2\pi n_2}, \quad (39)$$

where λ and ω are the wavelength and frequency of radiation, P_s is the soliton power, D is the group-velocity dispersion (GVD), β and A_{eff} are the propagation constant and the effective waveguide mode area, n_2 is the nonlinear refractive index of the fiber material, and c is the speed of light in vacuum.

The soliton solution to equation (37) is written out as $u = \text{sech } t \exp(iz/2)$. The pulse width of such a soliton, defined at the half-maximum of its temporal power profile, is $\tau = 1.763t_s$.

The retarded nonlinear response of the medium is included in the model through the following transformation of the nonlinear term on the right-hand side of equation (37) [48, 53]:

$$|u|^2 u \rightarrow u(t) \int f(\eta) |u(t-\eta)|^2 d\eta, \quad (40)$$

where $f(\eta)$ is the real function governing the Raman response of the fiber material. The Fourier transform of this function recovers the optical susceptibility of the medium (see Section 2):

$$\chi(\Omega) = \int f(\eta) \exp(i\Omega\eta) d\eta.$$

The imaginary part of this susceptibility, in turn, controls the Raman gain: $g_R(\Omega) = 2 \text{Im}[\chi(\Omega)]$.

Spectral transformation of equation (37) subject to the replacement (40) yields the following expression for the SSFS rate in units of THz km⁻¹ [53]:

$$\frac{dv}{dz} \approx -\frac{\mu\lambda^2 D}{t_s^3} \int_0^\infty \Omega^3 \frac{R(\Omega/2\pi t_s)}{\sinh^2(\pi\Omega/2)} d\Omega, \quad (41)$$

where μ is a constant factor, and $R(\Omega/2\pi t_s) = \alpha_R(\Omega)$.

A linear approximation of the function $R(\xi)$ [$R(\xi) \approx 0.492(\xi/13.2)$ for fused silica] gives the key expression of the Gordon model, allowing calculation of the SSFS rate [53]:

$$\frac{dv}{dz} \approx -\frac{\kappa_G}{\tau^4}, \quad (42)$$

where $\kappa_G = \kappa_0 \lambda^2 D$ is a constant coefficient in the Gordon model. For $\lambda = 1.5 \mu\text{m}$ and $D = 15 \text{ ps nm}^{-1} \text{ km}^{-1}$, equation (42) gives dv/dz (THz km⁻¹) $\approx 0.0436/\tau^4$ [53].

The Gordon formula played the key role in identifying significant tendencies of SSFS and in explaining interesting aspects of this phenomenon. Optical fibers of a new type—photonic-crystal fibers (PCFs) [69–79]—can radically enhance the SSFS rate [80, 81] due to the strong confinement of the laser field in an ultrasmall-area core of a specifically designed PCF. Unique regimes of soliton transmission supported by PCFs enable the creation of SSFS-based frequency-tunable fiber sources for nonlinear Raman spectroscopy and microscopy [82–89], as well as for optical detection of neuronal activity in the living brain [90]. Specifically designed PCFs can provide an efficient, smoothly tunable frequency conversion of low-power few-cycle optical pulses [91] and allow an all-optical pump–seed synchronization in optical parametric chirped-pulse amplification of few-cycle field waveforms [92]. An adequate description of the soliton self-frequency shift in such fibers requires an extension of the analysis beyond the Gordon formula. Numerical analysis of the generalized NSE with due regard for the retarded nonlinearity (the Raman response of the medium) suggests a deceleration of the frequency shifting of a soliton [93–95], as well as an ultrashort pulse of a more general form [54] in a certain phase of pulse propagation in a fiber. This effect can be employed to stabilize the SSFS and to reduce its sensitivity to fluctuations in the power of input laser pulses [96].

8. Soliton fiber sources of extremely short electromagnetic pulses

Development of compact and efficient sources of ultrashort light pulses is one of the main challenges of optical technologies [13, 79]. New types of optical fibers—micro- and nanostructure fibers [76–79, 97]—offer new solutions for the creation of highly efficient fiber-format short-pulse sources [65]. Photonic-crystal-fiber-based lasers can generate light pulses within a broad range of pulse widths and pulse energies [98–102]. Because of the limited gain band of active fiber components, few-cycle light pulses are extremely difficult to generate directly at the output of a fiber-optic laser system. In this context, PCF-based pulse compressors stir up heightened interest as a promising strategy for fiber-format pulse shortening [79, 103–108]. With such fibers, a high nonlinearity can be advantageously combined with tailored dispersion to enable compression of light pulses to pulse widths as short as a few femtoseconds [109–111]. Large-mode-area PCFs [103, 112–114] and hollow-core photonic-band-gap fibers [105, 115], on the other hand, allow compression of high-power light pulses.

Fiber-optic pulse compressors based on soliton dynamics of an electromagnetic field are well known in optical technologies. In such a system, a light pulse with an initial dimensionless energy of $2W^2$ propagates in an anomalously dispersive optical fiber, evolving toward a j th-order optical soliton (j is an integer) with a pulse width $\tau_j = \tau_0/2\xi_j$ [14], where $\xi_j = W - j + 0.5$ is the eigenvalue of the j th-order soliton. It is straightforward to see from the expression for the pulse width of the j th-order soliton that, for $\xi_j > 1/2$, the soliton arising as a result of this field dynamics is shorter than the input pulse, enabling soliton pulse compression.

The soliton dynamics of few- and single-cycle pulses is typically much more complicated, involving shock-wave formation and effects related to the inertia of optical nonlinearity. Evolution of the temporal envelope $A = A(z, t)$ of such pulses can be described with the use of the generalized nonlinear Schrödinger equation (GNSE) [14, 47]:

$$\begin{aligned} \frac{\partial A(z, \tau)}{\partial z} = & i \sum_{k=2}^7 \frac{i^k}{k!} \beta_k \frac{\partial^k A}{\partial \tau^k} + i\gamma_0 \left(1 + \frac{i}{\omega_0} \frac{\partial}{\partial \tau} \right) \\ & \times \left(A(z, \tau) \int_{-\infty}^{\infty} R(t) |A(z, \tau - t)|^2 dt \right), \end{aligned} \quad (43)$$

where z is the coordinate along the propagation direction of the light field, τ is the time in the retarded frame of reference, $\beta_k = \partial^k \beta / \partial \omega^k$ are the coefficients in the Taylor-series expansion of the propagation constant β about the central frequency of the light field, γ_0 is the coefficient of optical nonlinearity, and ω_0 is the central frequency of the light pulse. The function $R(t)$ includes both the electron (Kerr type) and phonon (Raman type) parts of optical nonlinearity [47, 48]:

$$R(t) = (1 - f_R) \delta(t) + f_R \Theta(t) \frac{\tau_1^2 + \tau_2^2}{\tau_1 \tau_2} \exp\left(-\frac{t}{\tau_2}\right) \sin\left(\frac{t}{\tau_1}\right), \quad (44)$$

where f_R is the fraction of retarded nonlinearity in the overall nonlinear-optical response, $\delta(t)$ is the delta function, $\Theta(t)$ is the Heaviside step function, and τ_1 and τ_2 are the characteristic time constants of the Raman response. For fused silica fibers [48], one obtains $f_R \approx 0.18$, $\tau_1 \approx 12.5 \text{ fs}$, and $\tau_2 \approx 32 \text{ fs}$.

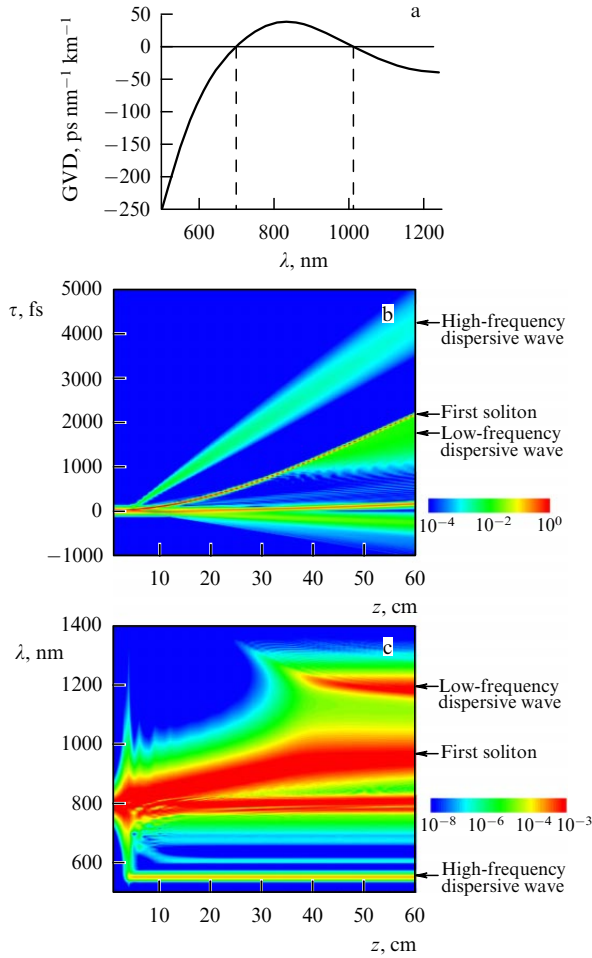


Figure 5. (a) The spectral profile of group-velocity dispersion of a highly nonlinear photonic-crystal fiber. Temporal (b) and spectral (c) dynamics of a light pulse in a fiber with such a GVD profile.

In Ref. [111], equations (43) and (44) were applied to analyze the dynamics of ultrashort light pulses in highly nonlinear PCFs. The input pulse in simulations is defined as

$$A(\tau) = A_0 F^{-1} \left[\exp \left(\frac{iC_0 \omega^2}{2} \right) \frac{\tau_0}{2} \operatorname{sech} \left(\frac{\pi}{2} \tau_0 \omega \right) \right], \quad (45)$$

where A_0 is the initial amplitude of the pulse envelope normalized in such a way that

$$W_0 = \int |A(\tau)|^2 d\tau, \quad (46)$$

where W_0 is the input pulse energy, $F^{-1}[\cdot]$ is the inverse Fourier transform, $\tau_0 \approx \tau_{\text{FWHM}}/1.76$, τ_{FWHM} is the pulse width defined as the full width at half maximum (FWHM), and C_0 is the chirp parameter of the input laser pulse.

We will consider an input pulse with a pulse width of 50 fs, an input energy of 70 pJ, and a central wavelength of 793 nm, and assume that such a pulse is launched into a fiber with a dispersion profile (Fig. 5a) typical of highly nonlinear PCFs [75–79]. The dispersion profile considered displays two zeros of group-velocity dispersion (GVD), with the long-wavelength zero-GVD point defining the red edge of the anomalous dispersion region. Such a shape of the GVD profile is observed in some highly nonlinear PCFs. As shown by earlier

work [116, 117], fibers with two zero-GVD points allow a cancellation of soliton self-frequency shift under certain conditions.

Figure 5b presents the temporal and spectral dynamics of the light pulse propagating in a fiber with the GVD profile shown in Fig. 5a. As can be seen from the results of these simulations, the initial phase of field evolution in the fiber involves temporal pulse compression. Since the soliton number of the input pulse is $N = (\gamma_0 P_0 \tau_0^2 / |\beta_2|)^{1/2} \approx 2.7$, with $P_0 = W_0(2\tau_0)^{-1}$ being the input peak power, the initial pulse-compression stage is followed by a phase where the pulse decays into several quasisolitonic transients. Each of these transients undergoes a red shift due to the Raman effect and radiates excessive energy in the form of dispersive waves in the short-wavelength range [118].

The soliton with the highest energy and shortest pulse width experiences the largest frequency shift. As this soliton gets shifted against the fiber dispersion profile, dispersive waves emitted by this soliton also change their frequency. When the soliton approaches the long-wavelength edge of the anomalous dispersion region, a long-wavelength branch of dispersive waves appears, as shown by Skryabin et al. [116], in the radiation spectrum, first decelerating and then completely suppressing the soliton frequency shift.

Along with soliton frequency shift suppression, a fiber with a dispersion profile featuring two zero-GVD points enables an efficient compression of a light pulse. The minimum pulse width of the soliton with the highest power may be estimated as $\tau_s \approx \tau_{\text{FWHM}}/1.76 \approx 9.3$ fs. The soliton pulse width and the soliton energy defined with the use of a standard procedure for evaluating the parameters of the solitonic part of the field fit well the relation

$$\tau_s = 2|\beta_2(\omega_s)| [\gamma(\omega_s)W]^{-1}, \quad (47)$$

where ω_s is the central frequency of the soliton. Unlike the standard formula for the parameters of the fundamental soliton, formula (47) involves local parameters of a light pulse, which change as the soliton propagates along the fiber due to the soliton self-frequency shift.

Results of simulations presented in Fig. 6 illustrate soliton pulse compression in a highly nonlinear PCF yielding sub-10-fs light pulses. Figure 6a displays the soliton FWHM pulse width $\tau_{\text{FWHM}} \approx 1.76\tau_s$ and the ratio ε of the output soliton energy to the energy of the input pulse calculated as functions of the initial pulse width. These simulations show that, as long as the fiber length is chosen in such a way as to provide the same soliton frequency shift for input pulses with different initial pulse widths, the soliton pulse width at the output of the fiber is virtually independent of the initial pulse width τ_0 within a broad range of τ_0 values (from 30 to 200 fs). For input pulses with $\tau_0 > 250$ fs, however, the fiber length needed to provide the invariance of the soliton frequency shift becomes so large that the fiber loss ceases to be negligible. As the energy of the light pulse decreases because of the fiber loss, the output pulse becomes longer. Notably, Eqn (46) remains valid in this regime, as well (see also Figs 6b–e).

Results of simulations presented in Fig. 7 illustrate PCF-based compression of light pulses to single-cycle and subcycle field waveforms. Our analysis has been performed for an input pulse with a central wavelength of 1070 nm and an initial phase $\varphi(\omega) = (\alpha/2)[\omega/(2\pi) - \omega_0/(2\pi)]^2$, where α is the chirp parameter. The frequency profiles of dispersion and nonlinearity chosen for these simulations (shown in the inset

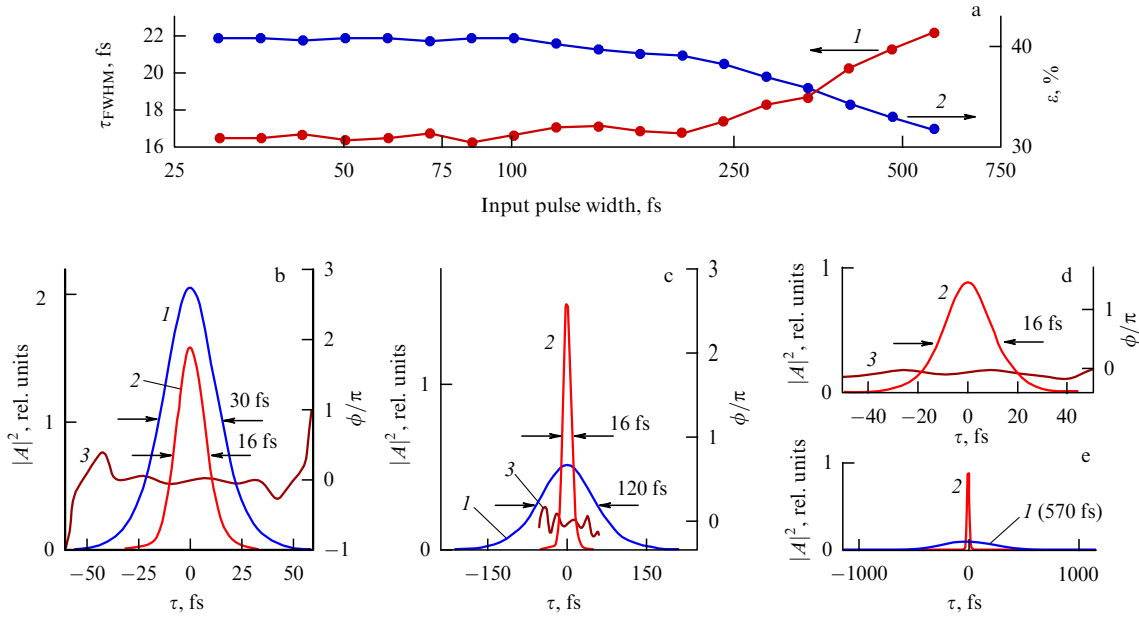


Figure 6. (a) The soliton FWHM pulse width τ_{FWHM} at the output of the fiber (1) and the ratio ε for this soliton (2) calculated as functions of the initial pulse width. (b–e) Results of simulations illustrating compression of pulses with different initial pulse widths to an output pulse width $\tau_s \approx \tau_{\text{FWHM}}/1.76 \approx 9.3$ fs in a highly nonlinear PCF: (1) profile of the input pulse envelope, (2) profile of the soliton envelope at the output of the fiber, and (3) profile of the phase ϕ of the output pulse. Panel (d) displays a blowup of the envelope and phase profiles of the fiber output for an input pulse with an initial pulse width of 570 fs. The fiber length was chosen in such a way as to provide a soliton shift to a central wavelength of 953 nm at the fiber output. The initial pulse energy is 70 pJ. The central wavelength of the input pulses is 793 nm. The GVD profile of the fiber is shown in Fig. 5a. The effective mode area is $S_{\text{eff}} = 3 \mu\text{m}^2$.

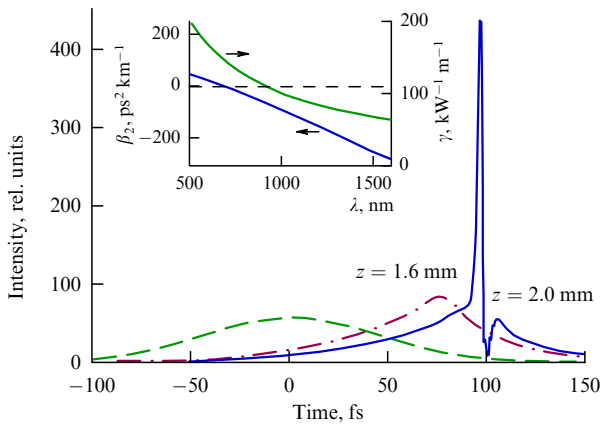


Figure 7. Temporal envelopes for an input pulse with a pulse width $\tau_0 = 30$ fs, a chirp $\alpha = -0.05$ ps², and an energy of 6.4 nJ (the dashed line), and a pulse at a distance $z = 1.6$ mm (dashed–dotted line) and 2.0 mm (solid line) from the input end of the fiber. The spectral profiles of fiber dispersion and nonlinearity are plotted in the inset.

to Fig. 7) are typical of highly nonlinear small-core PCFs. In such a fiber, the input light pulse is compressed to a pulse width of about 2 fs within a typical propagation length of about 2 mm (see Fig. 7). The minimum pulse width achieved with a highly nonlinear PCF and the fiber length needed for optimal pulse compression can be changed by varying the chirp of the input light pulse.

Because the analysis of soliton dynamics in a highly nonlinear fiber predicts formation of nominally subcycle light pulses, some comments on the adequacy of the GNSE [Eqn (43)] in this regime of field evolution may be in order. It should be noted here that, while the derivation of the NSE is

based on the slowly varying envelope approximation (SVEA), the framework of the GNSE is different [111, 119]. In contrast to SVEA pulse-evolution equations, which are valid only in cases where the local pulse width is much longer than the field cycle, $\tau_0 > T_0$, the validity of the GNSE does not impose an explicit limitation on the relationship between the pulse width and the field cycle, as this equation also involves non-SVEA terms describing high-order dispersion [$k > 3$ in Eqn (43)], shock-wave effects, and effects related to the inertia of optical nonlinearity (including Raman scattering).

The validity conditions for GNSE-based models of the spatio-temporal dynamics of ultrashort optical pulses are expressed by the following inequalities [111, 119]

$$\beta l_{\text{nl}}, \beta l_a, \beta l_d^{(k)}, \beta l_\psi \gg 1, \quad (48)$$

where $l_{\text{nl}} = (\gamma P)^{-1}$ is the nonlinear length, l_a is the length of attenuation due to absorption or leakage loss of waveguide modes, $l_d^{(k)} = \tau^k / |\beta_k|$ is the spatial scale whereon k th-order dispersion effects become significant, and $l_\psi = \lambda^{-1} (d\beta/d\lambda)^{-1}$. For pulses with a pulse width of ~ 2 fs and a peak power P not exceeding 0.2 MW, observed at $z = 2$ mm in Fig. 7, the most critical characteristic lengths in Eqn (48) for a fiber with $\beta_2 = -0.109$ ps² m⁻¹, $\beta_3 = 1.92 \times 10^{-4}$ ps³ m⁻¹, $\beta_4 = -2.58342 \times 10^{-7}$ ps⁴ m⁻¹ (corresponding to the dispersion profile shown in Fig. 5a), and $\gamma = 94$ kW⁻¹ m⁻¹ are estimated as $l_{\text{nl}} > 0.05$ mm, $l_d^{(2)} \approx 40$ μm , $l_d^{(3)} \approx 42$ μm , $l_d^{(4)} \approx 62$ μm , and $l_\psi \approx 15$ μm . All the conditions in inequalities (48) are thus satisfied with a large safety margin, $\beta l_{\text{min}} > 90$, for the fundamental fiber mode, where l_{min} is the minimum among l_{nl} , $l_d^{(k)}$, l_a , and l_ψ , indicating the applicability of the GNSE-based analysis to 2-fs pulses involved in simulations. The validity of GNSE type equations for the analysis of optical pulses with pulse widths on the order of T_0 under the

conditions of Eqn (48) was demonstrated earlier [111, 119] by a direct comparison of solutions to GNSE type equations with the results of numerical integration of Maxwell equations for the electric and magnetic fields.

Analysis of the soliton dynamics of ultrashort light pulses in highly nonlinear PCFs presented in this section suggests promising scenarios allowing pulse compression down to single-cycle field waveforms. We have derived simple analytical expressions relating the pulse width and the energy of ultrashort pulses generated through such field-evolution dynamics to the fiber dispersion and nonlinearity.

9. Molecular modulators and the synthesis of ultrashort field waveforms

Development of technologies capable of generating attosecond pulses of electromagnetic radiation [120–123] is one of the most significant achievements of optical physics over the past decade. Attosecond pulses provide unique tools for direct measurements of time constants of ultrafast electron dynamics in atomic and molecular systems [124–127], time-domain characterization of extremely short bursts of light field [128, 129], and control of ultrafast electron processes in the gaseous and condensed phases [130, 131].

The most widely applied method for the generation of attosecond pulses of electromagnetic radiation is based on high-order harmonic generation in gas jets [120–123, 132–135]. The shortest pulse width achieved to date is 80 as (0.08 fs) and is due to this approach [135]. Stimulated Raman scattering opens new routes toward the generation of ultrashort optical pulses, including attosecond field waveforms. Provided that appropriate phase-matching conditions are satisfied, Raman scattering by molecular vibrations or rotations in a gas medium or by phonons in solids pre-excited by narrow-band laser radiation [17, 33, 34] or ultrashort laser pulses [18, 35, 36] can efficiently generate multiple Stokes and anti-Stokes Raman sidebands in the spectrum of a laser field interacting with a Raman-active medium. In this regime, the Raman-active vibrations of gas molecules or phonons in a solid, phased with the laser field, play the role of elementary phase modulators shaping a probe pulse and transforming it into extremely short pulses of electromagnetic radiation. The length of interaction of the pump and probe pulses with the Raman-active medium can be increased by using gas-filled hollow waveguides [19]. Stimulated Raman scattering in a hollow waveguide filled with a Raman-active gas has been shown to allow the generation of optical pulses as short as a few femtoseconds [18]. Generation of subfemtosecond pulses is one of the next goals. Backward SRS in ionized media suggests ways toward a compression of high-energy light pulses, offering much promise for the generation of attosecond pulses with ultrahigh peak powers and field intensities [136, 137].

A Raman-active vibration with a frequency Ω can be efficiently excited by a light field whose spectrum includes frequency components ω_1 and ω_2 separated by an interval Ω (see Fig. 1). This can be achieved with the use of a biharmonic pump, where the phase excitation of vibrations is provided by a pair of narrow-band laser fields with carrier frequencies ω_1 and ω_2 . In the case of ultrashort light pulses, Raman excitation can be performed with a single optical pulse whose spectrum is broader than the vibrational frequency Ω .

The pump field drives Raman-active modes Q as it propagates through a Raman-active medium. A free decay

of these modes is described by the following expression:

$$Q(t) = Q_0 \exp\left(-\frac{t}{T_2}\right) \sin\left[\left(\Omega^2 - \frac{1}{T_2^2}\right)^{1/2} t\right], \quad (49)$$

where Q_0 is the amplitude of vibrations, which is proportional to the energy of the pump pulse, T_2 is the dephasing time of molecular vibrations, and Ω is the frequency of Raman-active vibrations.

The solution to the equation governing the evolution of the complex envelope $B(t, z)$ of the probe pulse entering the Raman-active medium with some delay with respect to the pump pulse in the plane-wave regime under conditions when the dephasing time T_2 substantially exceeds the period of Raman vibrations and the pulse widths is given by

$$B(\tau, z) = B(\tau, 0) \exp\left[-i\gamma \frac{\sin(\Delta K_{mm}z)}{\Delta K_{mm}} \sin(\Omega\tau + \Delta K_{mm}z)\right], \quad (50)$$

where $B(\tau, 0)$ is the envelope of the input probe pulse, and

$$\Delta K_{mm} = \frac{\Omega(1/v_2^n - 1/v_1^m)}{2} \quad (51)$$

is the parameter characterizing the mismatch of the group velocities v_1^m and v_2^n of the pump and probe pulses in waveguide modes m and n , $\tau = t - z/v_2^n$, and finally

$$\gamma = \frac{2\pi}{c} \omega_2 N Q_0 \frac{\partial \alpha}{\partial Q}, \quad (52)$$

where N is the concentration of Raman-active molecules in the gas, and $\partial \alpha / \partial Q$ is the derivative of the molecular polarizability with respect to the vibrational coordinate.

When the group-velocity mismatch ΔK_{mm} is small, expression (50) for the envelope of the probe pulse can be rewritten as

$$B(\tau, z) = B(\tau, 0) \sum_{s=-\infty}^{\infty} J_s(\gamma z) \exp(-is\Omega\tau), \quad (53)$$

where $J_s(x)$ is the s th-order Bessel function.

As can be seen from expression (53), the spectrum of the probe pulse consists of a superposition of equidistant Stokes and anti-Stokes sidebands with frequencies $\omega_s = \omega_2 + s\Omega$ ($s = 0, \pm 1, \pm 2, \dots$) separated by a spectral interval equal to the molecular vibrational frequency Ω . The number of these sidebands increases with the growth in the pump energy (leading to the increase in the parameter γ) and the interaction length. The minimum pulse width that can be achieved by compensating for the chirp of the pulse described by formula (53) is determined by the number M of Stokes and anti-Stokes components generated in the process of pulse propagation: $\tau \approx (2c\Delta k M)^{-1}$. With due regard for the properties of Bessel functions, the maximum value of M , in turn, is determined by the parameter γL (where L is the length of the Raman-active medium) in accordance with the approximate formula $M \approx \gamma L$. Thus, large interaction lengths are crucial for synthesizing ultrashort light pulses. The increase in the interaction length is, however, limited by group-delay effects and group-velocity dispersion. With an appropriate choice of hollow-fiber parameters, the waveguide dispersion component can reduce the group delay and group-

velocity dispersion for Stokes and anti-Stokes components within a broad spectral range. This is especially important for gases with high-frequency Raman-active vibrations, including molecular hydrogen.

10. Fiber-optic synthesizers of ultrashort light pulses

Soliton regimes of nonlinear-optical transformations of ultrashort laser pulses in fibers suggest attractive solutions to developing all-fiber synthesizers of few-cycle field waveforms. The key challenge to be addressed in the development of such synthesizers is to solve the problem of the coherent combining of Raman-shifted solitons generated as a part of the multisoliton dynamics of ultrashort pulses accompanied by soliton self-frequency shift. The synthesis of ultrashort field waveforms using coherent combining of solitons is illustrated by the results of calculations [138] presented in Fig. 8a. A laser pulse with an input pulse width of 100 fs and an energy of 30 nJ generates multiple solitons as it propagates through a large-mode-area PCF. Each soliton undergoes a frequency shift due to the Raman effect. The fringes observed in the PCF output spectrum result from the spectral interference of five red-shifted solitons with central frequencies $\nu_1 \approx 211$ THz, $\nu_2 \approx 198$ THz, $\nu_3 \approx 191$ THz, $\nu_4 \approx 164$ THz, and $\nu_5 \approx 149$ THz, pulse widths $T_1 \approx 22$ fs, $T_2 \approx 27$ fs, $T_3 \approx 29$ fs, $T_4 \approx 30$ fs, and $T_5 \approx 35$ fs, and energies of 1.6, 2.6, 2.9, 4.6, and 5.5 nJ. The second, third, fourth, and fifth solitons arrive at the PCF output with delay times of 220, 400, 1080, and 1890 fs relative to the first soliton. With a light modulator generating the five-step group-delay profile shown by the dashed line in Fig. 8a, the solitons coherently add up to synthesize a light pulse with a pulse width of about 10 fs. The temporal envelope and the chirp of the resulting pulse are displayed in the inset to Fig. 8a. The total radiation energy of this pulse, with the pedestal included, is 26.6 nJ. The energy of the central, 10-fs part of this pulse is about 12 nJ.

Figure 8b presents the results of experiments [138] performed with the use of Ti:sapphire laser pulses with an initial spectrum shown by the dashed line, and input energies of 0.6 and 7 nJ. As can be seen from this figure, frequency-shifted solitons produce high-visibility fringes in the spectral range from 880 to 980 nm. These fringes testify that each soliton has a flat spectral phase profile, suggesting the possibility of using large-mode-area PCFs for the synthesis of high-peak-power few-cycle optical pulses.

11. Synthesizers of tailored sequences of ultrashort light pulses for single-beam coherent anti-Stokes Raman scattering microspectroscopy

Methods of coherent Raman scattering offer unique opportunities for the investigations of ultrafast processes and implementation of novel methods of microscopy of physical, chemical, and biological systems [13, 21, 24, 25]. In the past decade, the tremendous potential of coherent anti-Stokes Raman scattering as a method of microspectroscopy and bioimaging has been demonstrated [26, 27]. The main advantages of this technique include a high spatial resolution, a high sensitivity, and a high selectivity related to the nonlinear-optical nature of the CARS process, the coherence of the CARS signal, and a precise tuning of light fields to a

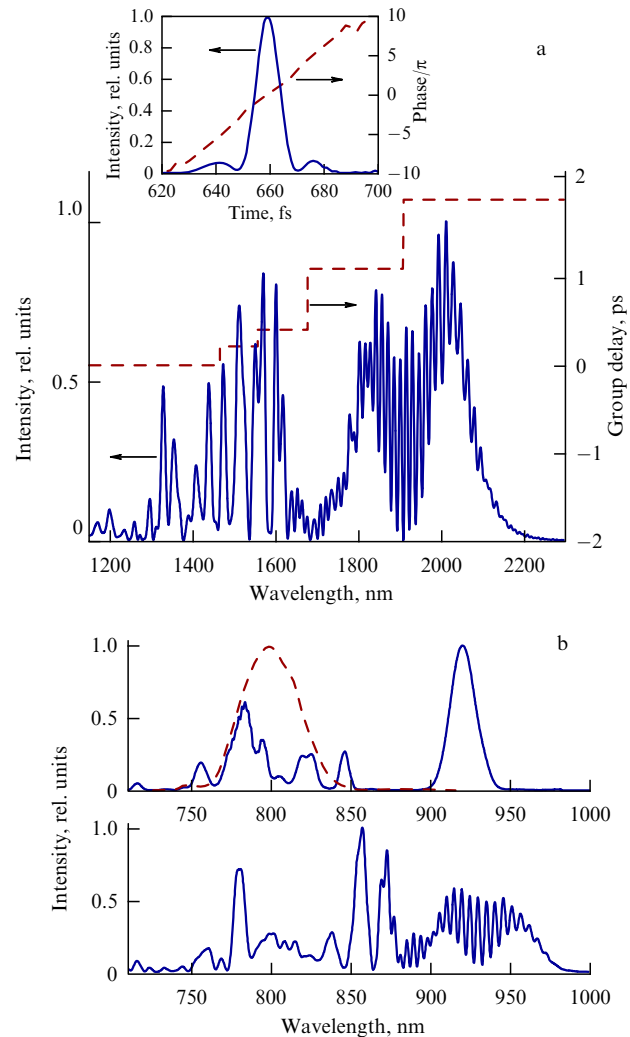


Figure 8. (a) The spectrum of a five-soliton pulse produced as a result of solitonic transformation of laser pulses with an input pulse width of 100 fs and an energy of 30 nJ in a large-mode-area photonic-crystal fiber. The inset shows the temporal envelope (solid line) and the phase (dashed line) of the light pulse synthesized through group-delay compensation as shown by the dashed line. (b) The spectra of the input Ti:sapphire laser pulses (dashed line) and pulses transmitted through a photonic-crystal fiber (solid line). The energy of input laser pulses equals 0.6 nJ (upper panel) and 7 nJ (lower panel).

resonance with Raman-active modes. Due to this unique combination of new options and advantages, CARS microscopy is emerging as a powerful tool of biomedical optics, allowing visualization of fine spatial structure details and *in vivo* studies of specific processes proceeding inside individual living cells [139].

CARS microspectroscopy involves excitation of Raman-active modes related to vibrational and rotational motions in molecules, as well as with electronic transitions in atomic and molecular systems. A Raman-active mode with a frequency Ω_0 is excited with light fields at frequencies ω_1 and ω_2 chosen in such a way that their difference is equal to Ω_0 . An inelastic scattering of a probe field with a frequency ω_3 from these coherently excited Raman excitations leads to the generation of a signal field at the frequency $\omega_a = \omega_1 - \omega_2 + \omega_3$, which carries spectroscopic information and yields high-contrast images of fine spatial structure details in an object under study.

In the widely used two-color CARS microspectroscopy, the frequency of the probe field ω_3 is equal to the pump frequency ω_1 . The frequency of the CARS signal is then equal to $\omega_a = 2\omega_1 - \omega_2 = \omega_1 + \Omega_0$. This modification of the CARS microspectroscopy requires only two laser sources—a source delivering radiation with a fixed frequency ω_1 , and a wavelength-tunable source generating a light field with the frequency ω_2 . As shown by recent work [82–89], fibers of a new type—photonic-crystal fibers (PCFs) [75–79]—can serve as convenient wavelength-tunable sources for CARS microscopes and spectrometers. Along with a substantial simplification and compactization of CARS systems, PCF-based wavelength-tunable sources and frequency converters offer a new attractive fiber format of light sources for nonlinear-optical microspectroscopy.

CARS apparatus can be further simplified through the use of light pulses with special phase profiles. As shown by Dudovich et al. [140, 141], liquid-crystal spatial light modulators can provide the required phase profiles of ultrashort pulses, allowing CARS microspectroscopy to be implemented with a single laser beam. In this regime, coherent excitation of Raman modes is possible when (i) the spectrum of the laser field $\Delta\omega$ is sufficiently broad ($\Delta\omega \gg \Omega_0$), and (ii) the phase profile $\Phi(\omega)$ of the laser field meets the condition $\Phi(\omega) = \Phi(\omega - \Omega_0)$. Similarly to two-color CARS, single-beam CARS implementation can be substantially simplified, as recently shown by von Vacano et al. [88], through frequency conversion in PCFs. To date, however, the spectral phase profile of the laser field required for a selective Raman excitation was synthesized by using spatial light modulators. We will show below in this section that a PCF operated in the regime of modulation instability (MI) can combine functions of a fiber component for efficient spectral transformation of laser fields and a pulse shaper, enabling coherence-controlled Raman excitation and single-beam CARS microspectroscopy.

Modulation instability in optical fibers [14] is understood as an instability of a light field with respect to a weak modulation of the temporal field envelope within a certain range of modulation frequencies. This weak modulation of the field envelope can be induced by noise or a weak external signal. In the frequency domain, a parametric amplification of such a weak modulation of the field envelope gives rise to intense sidebands in the spectrum of the field. In the time domain, the stationary optical field tends to evolve into a sequence of short light pulses.

For light fields governed by the nonlinear Schrödinger equation, modulation instabilities develop in the range of frequencies [14]

$$\Omega < \Omega_c = 2 \left(\frac{\gamma P}{|\beta_2|} \right)^{1/2}, \quad (54)$$

where $\gamma = n_2\omega/(cS_{\text{eff}})$ is the optical nonlinearity coefficient, n_2 is the nonlinear refractive index, ω is the radiation frequency, c is the speed of light, and

$$S_{\text{eff}} = \frac{\left[\int_{-\infty}^{\infty} \int_{-\infty}^{\infty} |F(x, y)|^2 dx dy \right]^2}{\int_{-\infty}^{\infty} \int_{-\infty}^{\infty} |F(x, y)|^4 dx dy} \quad (55)$$

is the effective mode area, $F(x, y)$ is the transverse spatial field profile in the waveguide mode, $\beta_2 = \partial^2\beta/\partial\omega^2$, β is the

propagation constant of the waveguide mode, and P is the peak power of the laser pulse.

The maximum MI gain is achieved at the frequency

$$\Omega_m = \frac{\Omega_c}{\sqrt{2}} = \left(\frac{2\gamma P}{|\beta_2|} \right)^{1/2}. \quad (56)$$

Modulation instabilities can build up from the noise component of the light field, related to spontaneous emission [14], or can be induced by a weak external field [142]. For ultrashort laser pulses, MIs may originate from a parametric amplification of new spectral components generated as a result of spectral broadening induced by self-phase modulation (SPM) [143]. In the presence of another laser field, MIs can be caused by cross-phase modulation [144].

In the time domain, parametric amplification of the Stokes and anti-Stokes sidebands with frequencies $\omega_0 \mp \Omega_m$, generated as a result of modulation instability of a field with an initial central frequency ω_0 , translates into a formation of sequences of light pulses [14] separated by the time interval $T_m = 2\pi/\Omega_m$. As can be seen from formula (56), the time interval T_m can be tuned by varying the peak power of the light pulse, as well as by changing the dispersion and nonlinearity of the fiber. Modulation instabilities in standard fibers can transform pulses with a typical pulse width on the order of 100 ps into sequences of femtosecond pulses with subterahertz repetition rates [142].

To illustrate the main peculiarities of field transformations induced by MIs in optical fibers, we consider a light field

$$E(t) = E_0 \exp\left(-\frac{t^2}{\tau^2}\right) [a_1 \cos \omega_0 t + a_2 \cos(\omega_0 + \Omega) t + a_3 \cos(\omega_0 - \Omega) t] \quad (57)$$

consisting of three spectral components with central frequencies ω_0 and $\omega_0 \mp \Omega$, and amplitudes a_j ($j = 1, 2, 3$), which correspond to the central frequency of the input field ω_0 and the frequencies $\omega_0 \mp \Omega$ of sidebands induced by a modulation instability in a fiber. The Gaussian factor in expression (57) accounts for a finite pulse width τ of the temporal field envelope and, correspondingly, nonvanishing bandwidths of all the spectral components involved in the MI type parametric process.

To calculate the Raman response of a molecular system, we express the generalized molecular coordinate Q representing a molecular vibration or rotation or any other type of motion as

$$Q(t) = \int_0^\infty h(\eta) F(t - \eta) d\eta, \quad (58)$$

where $h(\eta)$ is the relevant Green's function, and F is the driving force.

The Hamiltonian of a system with a polarizability α in a laser field E is written as

$$H = H_0 + V, \quad (59)$$

where H_0 is the field-free Hamiltonian, and

$$V = -\alpha(Q)E^2$$

is the Hamiltonian governing the Raman interaction of the mode represented by the generalized coordinate Q with the field E .

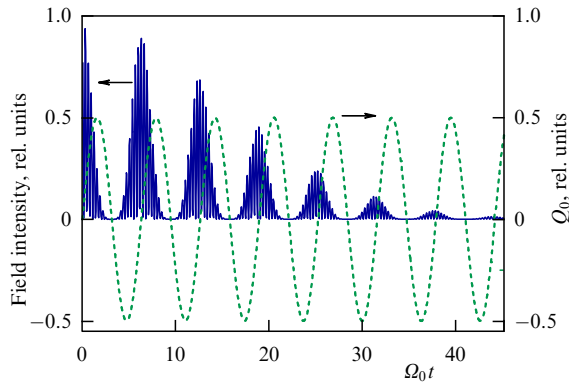


Figure 9. The driving force $F(t)$ induced by a light field (57) with $\tau = 30/\Omega_0$ and $a_1 = 2a_2 = 2a_3$ (the solid line) providing an in-phase excitation of a Raman mode $Q(t) \propto \sin(\Omega_0 t)$ (dashed line).

The driving force in formula (58) is then given by

$$F = -\frac{\partial V}{\partial Q} = \frac{\partial \alpha}{\partial Q} E^2. \quad (60)$$

The optical response for a broad class of molecular systems can be described in terms of a damped harmonic oscillator model, yielding the following expression for the Green's function in formula (58):

$$h(\eta) \propto \exp(-\Gamma\eta) \sin(\bar{\Omega}\eta), \quad (61)$$

where $\bar{\Omega} = (\Omega_0^2 - \Gamma^2)^{1/2}$, Ω_0 is the mode frequency, and Γ is the damping rate.

Given the equality $\Omega = \Omega_0$, the driving force (60) generated by the light field (57) (shown by the solid line in Fig. 9) provides a coherent selective excitation of the Raman mode with the frequency Ω_0 (the dashed line in Fig. 9). For long laser pulses with $\tau \gg \Gamma^{-1}$, integration in formula (58) yields a harmonic molecular response

$$Q(t) = Q_0 \sin(\Omega t + \phi),$$

where ϕ is the phase of the laser-driven mode. The frequency dependence of the amplitude Q_0 of such a response is given by a Lorentzian profile:

$$Q_0 \propto [(\Omega - \Omega_0)^2 + \Gamma^2]^{-1/2}.$$

Due to their high optical nonlinearity and tailored dispersion, photonic-crystal fibers substantially enhance parametric transformations of ultrashort laser pulses [145–147]. Dispersion profiles of such fibers are often quite complicated and nonlinear coefficients are very high. Expressions (54) and (56) under these conditions can offer only qualitative insights into the main tendencies of MI type parametric interactions of ultrashort light pulses. The details of the spectral and temporal evolution of light fields in such fibers in the MI regime can be understood through the employment of numerical simulations, including high-order dispersion effects and the retarded (Raman) part of optical nonlinearity. An adequate framework for such an analysis is provided by the generalized nonlinear Schrödinger equation (43). Numerical simulations were performed for laser pulses with a central wavelength of 1070 nm, an initial pulse width of 2 ps, an input peak power of 10 kW, and an input spectrum shown by line 1 in Fig. 10a. The group-velocity dispersion

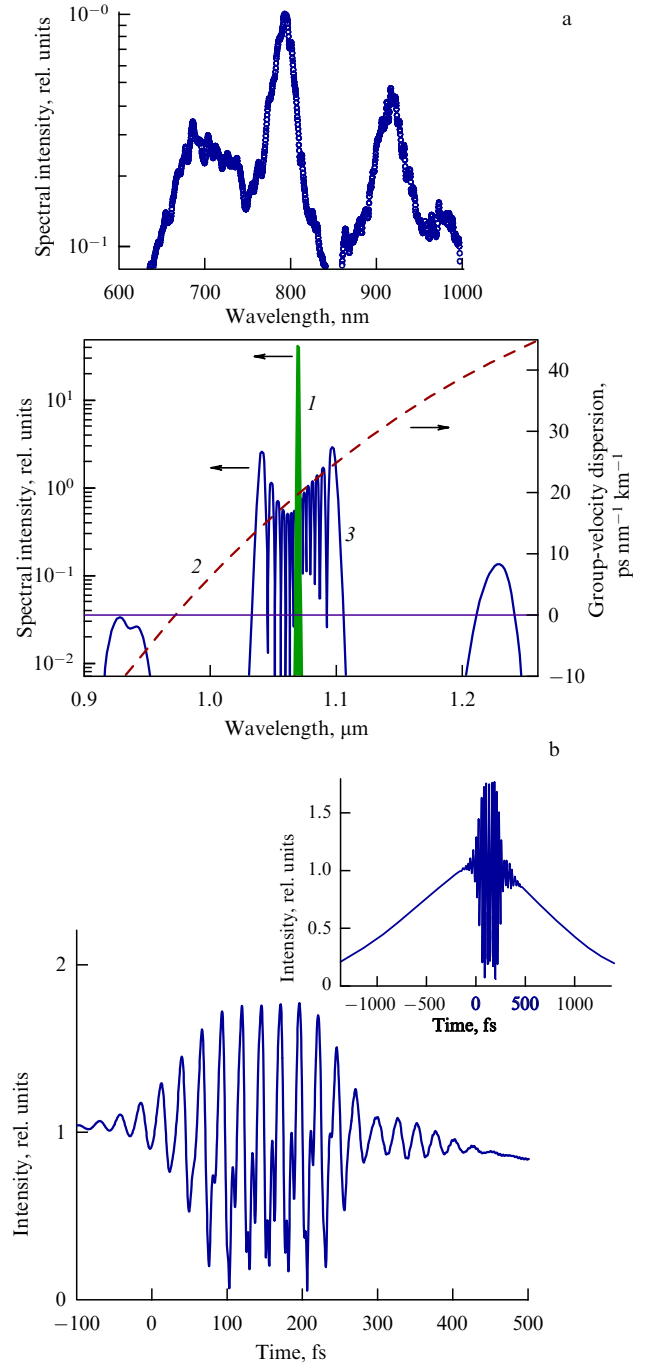


Figure 10. (a) The spectrum of the input field (1), the spectral profile of group-velocity dispersion of the fiber (2), and the spectrum of the field transmitted through a 12-cm PCF (3). The input pulses have a central wavelength of 1070 nm, a pulse width of 2 ps, and a peak power of 10 kW. The inset displays a typical spectrum of femtosecond Ti:sapphire laser pulses transmitted through a silica PCF with a nonlinear coefficient $\gamma \approx 50 \text{ W}^{-1} \text{ km}^{-1}$. The input laser pulse width is 50 fs. The initial pulse energy is 0.5 nJ. (b) Field intensity envelope of a laser pulse with a central wavelength of 1070 nm, an input pulse width of 2 ps, and an initial peak power of 10 kW transmitted through a 12-cm PCF. The general view of the output pulse envelope is shown in the inset.

profile of an optical fiber (line 2 in Fig. 10a) was defined in a form typical of PCF dispersion. Figures 10a and 10b display the numerical solution of equation (43) for the intensity spectrum and the intensity envelope of the field at the output of a 12-cm fiber. Modulation instability induces intense

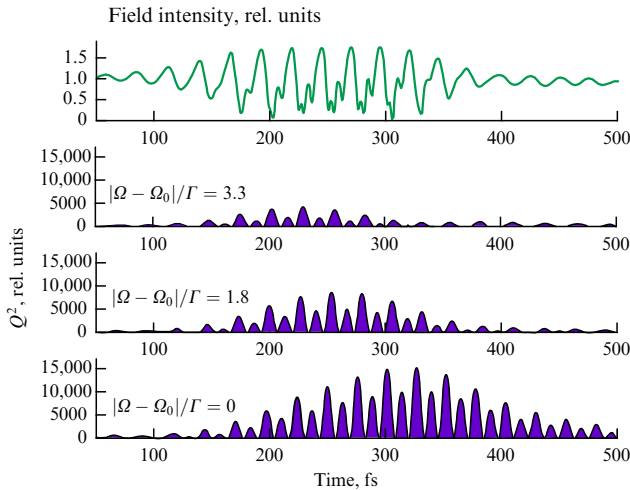


Figure 11. Field intensity at the output of the PCF (the upper panel) and the amplitude of the Raman response for the frequency detuning $|\Omega - \Omega_0|/\Gamma = 0, 1.8, 3.3$ (from top to bottom); $\Omega_0/\Gamma \approx 24.2$.

sidebands in the output spectrum (Fig. 10a). In the time domain, this corresponds to the generation of a periodic sequence of short light pulses (Fig. 10b). The repetition rate of these pulses is controlled by the dispersion and nonlinearity of the fiber, and the peak power of the laser pulses. Due to the high nonlinearity of the PCF, periodic sequences of sub-10-fs pulses can be generated in the regime considered (Fig. 10b).

Figure 11 presents the response Q of a Raman-active mode to the field generated at the output of a 12-cm photonic-crystal fiber as a result of MI type parametric transformation of light pulses with an initial pulse width of 2 ps, a central wavelength of 1070 nm, and an input peak power of 10 kW [148]. As can be seen from Fig. 11, the sequence of light pulses produced by the photonic-crystal fiber can provide selective excitation of Raman-active modes with the frequency $\Omega_0 = \Omega$. In this regime, MI type parametric interaction in a PCF not only provides an efficient spectral transformation of the laser field, but also synthesizes a spectral phase profile $\Phi(\omega)$ that meets the condition $\Phi(\omega) \approx \Phi(\omega - \Omega_0)$ necessary for an in-phase excitation of a Raman-active mode [140, 141].

Experiments [145–147] confirm that modulation instabilities in PCFs can efficiently generate intense sidebands in the spectra of ultrashort laser pulses, providing the frequencies Ω falling within the region of characteristic frequencies of vibrational and rotational Raman-active molecular modes. The inset to Fig. 10a presents a typical spectrum of femtosecond Ti:sapphire laser pulses transmitted through a highly nonlinear silica PCF [146]. The spectrum of the fiber output features intense sidebands separated by a frequency interval $\Omega/2\pi \approx 50$ THz from the central frequency of the laser field.

In earlier experiments on single-beam CARS microscopy [88], optimally shaped light fields for a selective excitation of molecular vibrations were produced through spectral broadening in a PCF and pulse shaping by a liquid-crystal spatial light modulator. The analysis presented in this section suggests that PCFs with properly chosen dispersion and nonlinearity parameters can simultaneously generate a richer spectral content and serve as a pulse shaper synthesizing optimal phase profiles for a selective resonant excitation of Raman-active modes. Photonic-crystal fibers thus allow the development of compact and efficient fiber components

for coherence-controlled Raman excitation and single-beam CARS microscopy. In contrast to periodic sequences of ultrashort light pulses that can be readily produced as a result of coherent superposition of optical fields with different carrier frequencies, the pulse-train synthesizers considered here allow the time intervals between the pulses to be controlled by varying the peak power of input laser pulses and enable pulse-train synthesis in an all-fiber format.

12. Coherent Raman scattering of ultrashort light pulses by optical phonons

Coherent Raman scattering is attracting much attention as a method for the excitation of ultrafast optical phonon modes in solids. Coherent Raman techniques using ultrashort laser pulses help in identifying physical scenarios of electron-phonon interactions in solids [149], in understanding ultrafast lattice dynamics induced by phase transitions [150], and in implementing a coherent control of optical phonons [151, 152]. Coherent Raman scattering of ultrashort pulses by optical phonons in solids also suggests a promising method for the synthesis of ultrashort light pulses through the phased generation of multiple Raman sidebands [153].

Figure 12 sketches an experiment [154] implementing coherent Raman excitation of optical phonons in synthetic diamond films. The laser system used in these experiments consists of a femtosecond Cr:forsterite laser oscillator and photonic-crystal fibers for controlled spectral and temporal transformation of ultrashort light pulses. With a 10-W pump provided by an ytterbium fiber laser, the specifically designed long-cavity Cr:forsterite laser oscillator delivers 340-mW light pulses with a central wavelength of 1.25 μm and a pulse width of 50–70 fs at a repetition rate of 18 MHz. The Cr:forsterite laser output was spectrally compressed in a nonlinear fiber and was employed as a pump field (frequency ω_1) for coherent Raman excitation of optical phonons. A frequency-tunable Stokes field (frequency ω_2) is generated through a soliton self-frequency shift of the Cr:forsterite laser output in a properly designed photonic-crystal fiber (PCF1 in Fig. 12). The central wavelength of the soliton fiber output is tuned by varying the power of femtosecond laser pulses at the input of the fiber. The frequency-shifted soliton output of the PCF was characterized by means of cross-correlation frequency-resolved optical gating (XFROG), which was implemented by mixing the PCF output with reference pulses from the Cr:forsterite laser. Typical XFROG traces of a frequency-shifted PCF output with different input peak powers are presented in Fig. 13a. As can be seen from these measurements, the PCF output is tunable within the range of wavelengths from 1.35 to 1.75 μm , with its pulse width varying within the range of 55–65 fs for different output wavelengths.

The difference between the central frequencies of the pump and Stokes fields, $\omega_1 - \omega_2$, was scanned through the Raman resonance of the triply degenerate zone-center $\Gamma^{(25+)}(F_{2g})$ symmetry optical phonon with the frequency $\Omega_p/(2\pi c) \approx 1332$ cm^{-1} in a synthetic diamond film. A typical spectrum of spontaneous Raman scattering of a diamond film is presented in inset I to Fig. 14. Phonon excitation is detected with the use of the probe field (frequency ω_3), which undergoes coherent Raman scattering off the optical phonons driven by the pump and Stokes fields. The anti-Stokes signal at the frequency $\omega_a = \omega_1 - \omega_2 + \omega_3 = \Omega_p + \omega_3$ generated as a result of this CARS process is used to study the

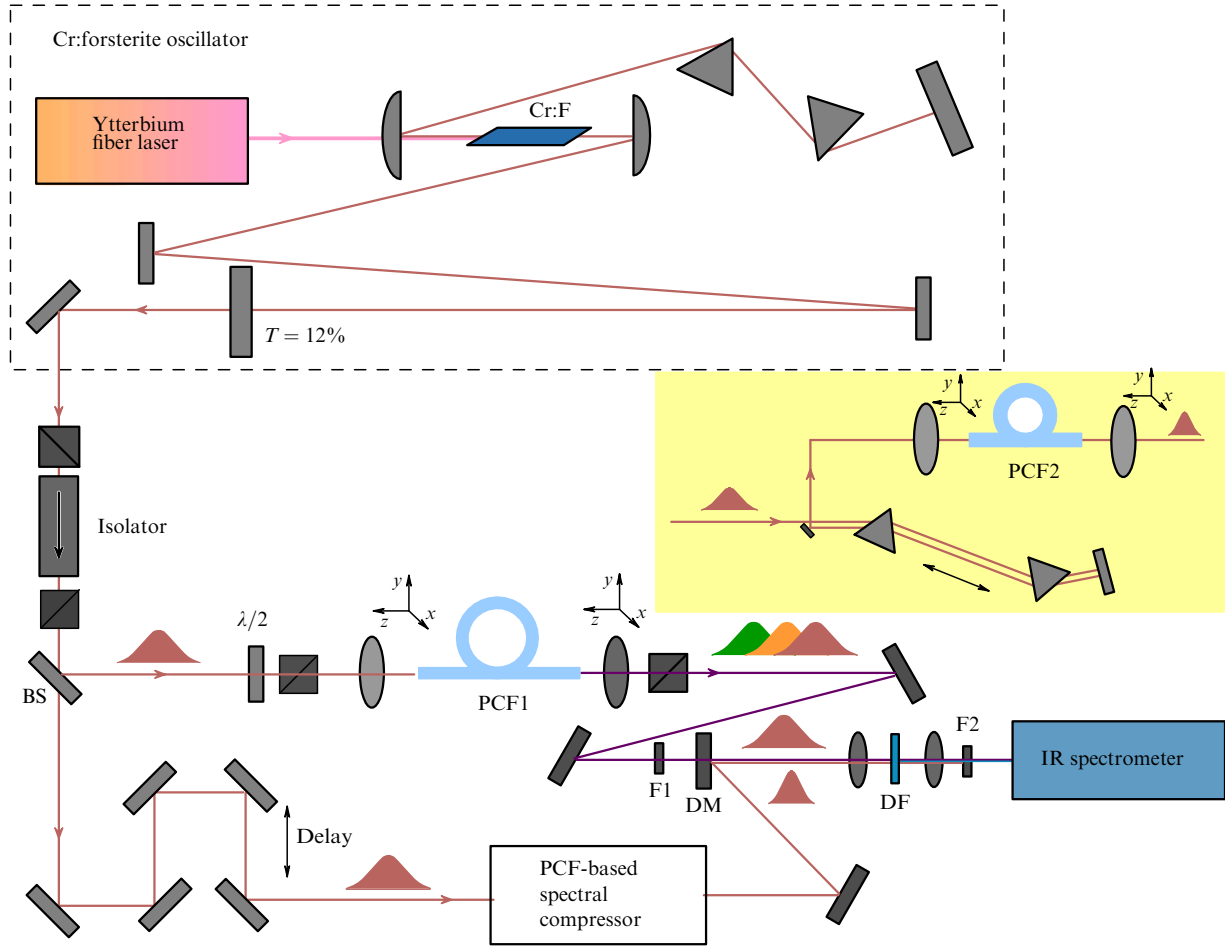


Figure 12. Schematic of the CARS spectrometer: Cr : F, femtosecond Cr:forsterite laser; BS, beam splitter; PCF1, PCF2, photonic-crystal fibers; F1, F2, filters; DM, dichroic mirror, and DF, synthetic diamond film. Diagram of a PCF-based spectral compressor is shown in the inset.

excitation and decay of optical phonons. In experiments [154], the probe pulses were produced by means of the spectral compression [155, 156] of Cr:forsterite laser pulses in a photonic-crystal fiber (PCF2 in Fig. 12). For efficient spectral compression, the light pulses were negatively prechirped with a prism pair, which stretched the pulses to approximately 700 fs, before they were launched into the PCF. Spectral compression ratios (defined as the ratio of the bandwidth of the fiber output to the bandwidth of input laser pulses) at the level of 3.5–4.0 provided an adequate spectral resolution in CARS measurements and helped suppress the nonresonant background due to off-resonant four-wave mixing processes.

Typical spectra of the anti-Stokes signal measured by scanning the Stokes frequency near the Raman resonance with the optical phonon, $\omega_2 \approx \omega_1 - \Omega_p$, are shown in Fig. 14 [154]. The Raman line of the optical phonon in a synthetic diamond film is much broader (about 2.0 cm^{-1}) than the same line in natural diamond samples (1.65 cm^{-1} at a temperature of 300 K [157]). Coherent Raman spectroscopy can thus be employed for optical diagnostics of disorder in crystal systems. The CARS spectra presented in Fig. 14 display characteristic asymmetry, indicating the interference of resonant and nonresonant parts of the third-order nonlinear susceptibility $\chi^{(3)}$ (see Section 2).

To retrieve quantitative information on the properties of an optical phonon through an appropriate fitting procedure,

we represent the intensity of the anti-Stokes signal as

$$I(\omega_a) \propto \left| \iiint d\omega_1 d\omega_2 d\omega_3 \chi^{(3)} E_1(\omega_1) E_2^*(\omega_2) E_1(\omega_3) \times \delta(\omega_a - \omega_1 + \omega_2 - \omega_3) \right|^2, \quad (62)$$

where $E_1(\omega_{1,3})$ is the spectrum of the pump and probe fields, and $E_2(\omega_2)$ is the spectrum of the Stokes field. The fitting procedure was performed with the $E_1(\omega_{1,3})$ and $E_2(\omega_2)$ spectra as measured (see Figs 13, 14) at the output of PCF2 and PCF1, respectively. The credibility of the fitting procedure was verified by the agreement between the results of calculations and experimental spectra measured off the Raman resonance of the diamond film (CARS spectrum δ in Fig. 14, measured with the PCF1 output with spectrum δ in inset II to Fig. 14).

The nonlinear-optical susceptibility is represented (see Section 2) as a sum of a real nonresonant part $\chi_{nr}^{(3)}$ and complex resonant susceptibility with a Lorentzian spectral profile:

$$\chi^{(3)} = \chi_{nr}^{(3)} + \chi_r^{(3)} \frac{\Gamma_p}{2} \left[\Omega_p - (\omega_1 - \omega_2) + \frac{i\Gamma_p}{2} \right]^{-1}, \quad (63)$$

where $\chi_r^{(3)}$ is the amplitude of the resonant part of the nonlinear-optical susceptibility, and Γ_p is the optical phonon linewidth.

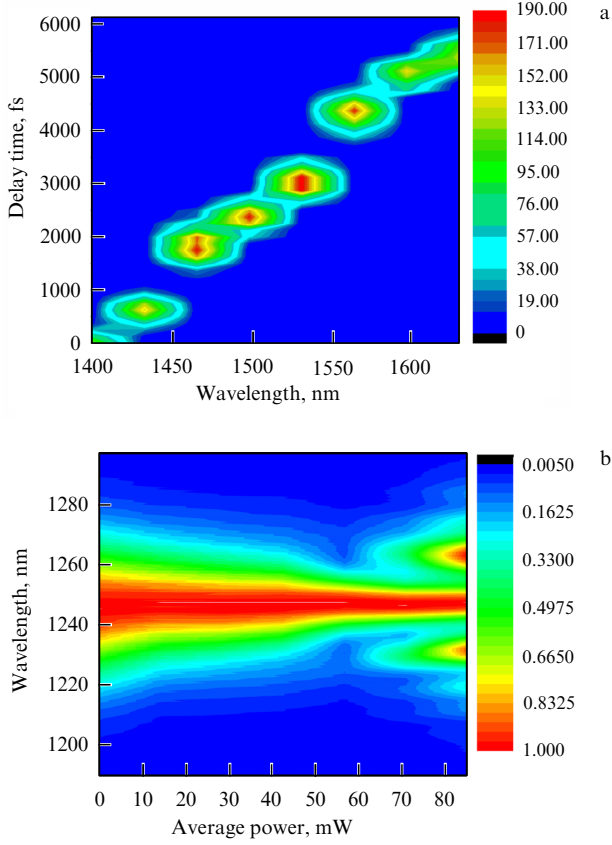


Figure 13. (a) A map showing X-FROG traces of the frequency-tunable PCF1 output. (b) Spectra of the output of the photonic-crystal fiber (PCF2) used for the spectral narrowing of Cr:forsterite laser pulses, measured as a function of the average power of input light pulses.

Then, setting $\Gamma_p/(2\pi c) \approx 2 \text{ cm}^{-1}$ and $\Omega_p/(2\pi c) \approx 1332 \text{ cm}^{-1}$, as dictated by spontaneous Raman spectra for the synthetic diamond films studied, and using $|\chi_r^{(3)}/\chi_{nr}^{(3)}|$ as the only fitting parameter, we find that the best fit for the experimental CARS spectra (see Fig. 14) is achieved with $|\chi_r^{(3)}/\chi_{nr}^{(3)}| = 17 \pm 2$. This value is a factor of 1.24 lower than the resonant-to-nonresonant susceptibility ratio found by Levenson et al. [158] for crystalline diamond with all the electric fields polarized along the crystallographic [110] direction. Nevertheless, this result points to a sufficiently strong Raman nonlinearity of synthetic diamond films, suggesting synthetic diamond as a promising material for the efficient frequency conversion of ultrashort laser pulses and the synthesis of few-cycle field waveforms through the generation of phased multiple Raman sidebands as a result of high-order SRS.

The time-domain nonlinear Raman response function of a diamond film can be recovered by taking the Fourier transform of the nonlinear susceptibility (63):

$$f(t) = (1 - f_R) \delta(t) + f_R H(t) \frac{\tau_1^2 + \tau_2^2}{\tau_1 \tau_2} \exp\left(-\frac{t}{\tau_2}\right) \sin\left(\frac{t}{\tau_1}\right), \quad (64)$$

where $\tau_1 = \Omega_p^{-1} \approx 4.0 \text{ fs}$, $\tau_2 = 2/\Gamma_p \approx 5.3 \text{ ps}$, and

$$f_R = \left(1 + \frac{\kappa \chi_{nr}^{(3)}}{\chi_r^{(3)}}\right)^{-1}$$

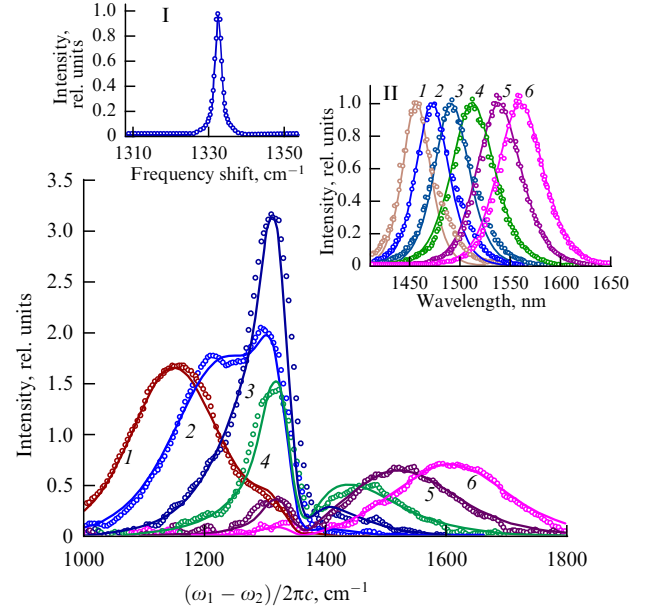


Figure 14. Spectra of the CARS signal from a synthetic diamond film. Pump and probe pulses are spectrally compressed with the use of a photonic-crystal fiber PCF2. Frequency-tunable Stokes pulses are generated through soliton self-frequency shift in a photonic-crystal fiber PCF1. The spectrum of spontaneous Raman scattering for the synthetic diamond film is shown in inset I. Inset II displays the spectra of the soliton PCF1 output (1–6) used to measure the respective CARS spectra (1–6). Experimental spectra are marked by open circles. The solid lines demonstrate the theoretical fits for CARS spectra with the respective Stokes spectra as shown by the solid lines in inset II, assuming a Lorentzian profile of the optical phonon line with $\Omega_p/(2\pi c) = 1332 \text{ cm}^{-1}$, $\Gamma_p/(2\pi c) = 2 \text{ cm}^{-1}$, and $|\chi_r^{(3)}/\chi_{nr}^{(3)}| = 17$.

is the fraction of the Raman part in the overall nonlinear response.

For the parameters of experimentally studied synthetic diamond films, we find $f_R \approx 2.48\%$. This agrees well with the value of $f_{R0} \approx 2.53\%$, retrieved from the CARS spectra of crystalline diamond [158]. The smallness of f_R , however, does not necessarily imply a weakness of the Raman response. The strength of the Raman response can be appreciated by calculating the SRS gain which can be expressed as $g_R = 4n_2 n_0 \omega (3c)^{-1} |\chi_r^{(3)}/\chi_{nr}^{(3)}|$, where n_0 is the refractive index. With a typical value of the Kerr-effect-related nonlinear refractive index of synthetic diamond, $n_2 \approx 5.4 \times 10^{-16} \text{ cm}^2 \text{ W}^{-1}$ at a wavelength of 800 nm, we find $g_R \approx 2.3 \text{ cm GW}^{-1}$, which is two orders of magnitude higher than the SRS gain of fused silica ($g_R \approx 0.01 \text{ cm GW}^{-1}$).

The optical nonlinearity of diamond films can be radically enhanced through an in-phase excitation of optical phonons with a sequence of ultrashort laser pulses. To illustrate this possibility, we assume that the pulse widths of optical pulses can be considered infinitely small on a typical time scale of the problem:

$$I(t) \propto I_0 \sum_{m=0}^M \delta(t - m\Delta t). \quad (65)$$

For an in-phase excitation of a phonon mode with a frequency Ω_p , the time interval Δt between the pulses in the sequence is taken equal to the oscillation period of the Raman-active mode, $\tau_v = 2\pi/\Omega_p$. The amplitude of the

Raman-active mode with the frequency Ω_p can then be found using a model of a damped harmonic oscillator with the frequency Ω_p and decay rate Γ_p . For $t > M\Delta t$, this amplitude is given by

$$Q_p(t) \propto \frac{I_0 M}{\Omega_p} \zeta \sin(\Omega_p t + \varphi_p), \quad (66)$$

where $\zeta = [1 - \exp(-M\Gamma_p\Delta t)][1 - \exp(-\Gamma_p\Delta t)]^{-1}$, and φ_p is the phase shift determined by a specific physical mechanism behind an electron–phonon coupling.

Provided that $\Gamma_p\Delta t \ll 1$, $M\Gamma_p\Delta t \gg 1$, and $\Delta t = \tau_v$, we have $\zeta \approx (2\pi\Gamma_p)^{-1}\Omega_p$. In this regime, the maximum enhancement of the nonlinear response related to Raman scattering by optical phonons is controlled by the Ω_p/Γ_p ratio. For synthetic diamond films studied in experiments [154], we find $\zeta \approx 110$. Thus, with a sufficiently long sequence of few-cycle laser pulses, the optical nonlinearity related to Raman scattering by optical phonons can be increased by more than two orders of magnitude.

13. Optical detection of ultrafast physical processes on the attosecond time scale

Raman scattering of ultrashort pulses through electronic transitions of atoms and molecules is of special interest for the investigation of ultrafast processes in atomic and molecular systems on the attosecond time scale. Methods of CARS spectrochronography have been successfully used for the analysis of excitation and population relaxation kinetics of atomic electronic states in gas and plasma media [24]. In particular, CARS provides a powerful tool for the detection of Raman-active transitions between hyperfine-structure levels of rare-earth atoms [159]. In combination with the selective Raman population of excited states in atomic hyperfine-structure levels, CARS opens up vast opportunities for optical metrology, as well as optical signal and data processing [160]. As one of the most recent trends, coherent X-ray Raman scattering is finding growing applications for the investigation of femto- and attosecond dynamics of vibrational wave packets in rapidly decaying excited states of molecular quantum systems [161].

Below in this section, we will discuss the potential of CARS as a technique for the optical detection and time-resolved analysis of autoionization phenomena in atomic and molecular media. Autoionization processes play an important role in multielectron dynamics in a broad class of quantum systems, including such fundamentally important and practically significant processes as the autoionization of water molecules and Auger decay of vacancies in the inner electronic shells of atoms [162]. The potential of coherent Raman spectroscopy for the investigation of autoionization dynamics on the nanosecond time scale was experimentally demonstrated about two decades ago [24, 163]. In recent experiments, unique direct measurements of Auger-decay times have been performed with attosecond time resolution for vacancies in the inner electronic shells of atoms [122, 125]. The experimental approach implemented in these experiments involves measurements of the spectrum of electron emission as a function of the delay time between an attosecond X-ray pulse producing a vacancy in an inner atomic shell and an ultrashort laser pulse controlling the momentum distribution of emitted electrons. Coherent Raman scattering offers new possibilities for the detection

and analysis of autoionization processes in the format of an all-optical experiment.

An autoionizing (AI) state of a many-electron system, originating from the interference of the continuum wave function ψ_E of energy E and an electron bound state φ , can be described within the framework of the Fano model [164, 165]:

$$\Psi_E = \frac{\sin \Delta}{\pi V_E} \Phi - \psi_E \cos \Delta, \quad (67)$$

where

$$\Phi = \varphi + \text{v.p.} \int \frac{V_{E'} \psi_{E'}}{E - E'} dE' \quad (68)$$

is the wave function of the bound state modified by coupling with the continuum states, which is expressed through the principal-value integral, Δ is the phase shift of the radial part of the Fano state, $V_E = \langle \varphi | H | \psi_E \rangle$, and H is the Hamiltonian of the electron system.

Autoionization gives rise to the emission of photoelectrons with a Fano–Beutler spectrum [164 – 166]:

$$\sigma(\varepsilon) = \frac{(q + \varepsilon)^2}{1 + \varepsilon^2}, \quad (69)$$

where $\varepsilon = (E - E_0)/\Gamma$, E_0 is the energy that determines the center of the AI feature, $\Gamma = \pi |V_E|^2$ is the full width of the AI resonance, and

$$q = \frac{\langle \Phi | T | \varphi_i \rangle}{\pi V_E^* \langle \psi_E | T | \varphi_i \rangle} \quad (70)$$

is the Fano parameter [164], with T being the dipole-moment operator.

To examine the linear-optical response of an AI state in the time domain, we employ the standard expression for a Fano resonance in terms of the complex scattering amplitude:

$$f(\varepsilon) = \frac{q + \varepsilon}{1 - i\varepsilon}. \quad (71)$$

Fourier transform of the complex scattering amplitude given by formula (71) yields

$$f(t) = \frac{\Gamma}{\hbar} (q - i) \Theta(t) \exp\left(-i \frac{E_0}{\hbar} t\right) \exp\left(-\frac{\Gamma}{\hbar} t\right) + i\delta(t), \quad (72)$$

where $\Theta(t)$ is the Heaviside step function.

The linear-optical response function defined by formula (72) reflects the interference nature of AI states, originating from overlapping discrete and continuous states. This function includes a damped-oscillator part, representing bound–bound transitions, and a delta-function component [cf. Eqn (3) for the purely nonresonant electronic part of nonlinear-optical response], corresponding to transitions into the continuum.

The time-domain nonlinear-optical response of AI states can be calculated using perturbation theory [167, 168] or through the Fourier transform of the nonlinear-optical susceptibility of the form (9) with the sum over the intermediate states replaced by integration over the continuum

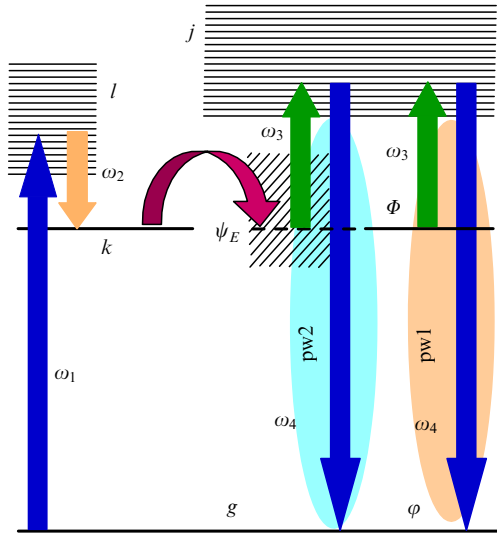


Figure 15. Coherent anti-Stokes Raman scattering through autoionizing states. The frequency difference $\omega_1 - \omega_2$ between an attosecond X-ray pulse and an ultrashort Stokes pulse is tuned to a resonance with a Raman type transition coupling the initial level g and an AI state k . The time-delayed pulse with the frequency ω_3 probes the Raman modes excited by the pump and Stokes pulses. Also shown are the manifolds of virtual levels l and j contributing to the nonlinear polarization of the medium, leading to the generation of the CARS signal. The AI state k is a result of interference of a modified discrete state Φ and a continuum state ψ_E . Raman transitions coupling the modified discrete state Φ and the continuum state ψ_E to the bound state g with the wave function ϕ form the interfering quantum pathways pw1 and pw2, respectively.

states. Analysis of the nonlinear-optical response of many-electron systems shows that the methods of coherent Raman scattering allow a separation of the interfering relaxation pathways for AI states of many-electron systems due to transitions into bound and free electronic states, as well as measuring the relevant time constants for such pathways with attosecond time resolution [161]. To illustrate this possibility, we consider a pair of interfering AI states excited through a Raman type process (Fig. 15) by an X-ray or ultraviolet attosecond pump pulse (frequency ω_1) and an ultrashort laser Stokes pulse (frequency ω_2). An AI state k in Fig. 15 originates from the interference of a modified quantum state Φ , belonging to the discrete spectrum, and a continuum state ψ_E . Raman transitions coupling the state Φ and the continuum state ψ_E to the bound state g with a wave function ϕ_g give rise to interfering pathways pw1 and pw2. A probe pulse in the considered scheme of CARS spectrochronography is used to study the decay of a packet of AI states prepared by the pump and Stokes pulses.

Figures 16a–c present the intensity of the CARS signal generated at the frequency $\omega_4 = \omega_1 - \omega_2 + \omega_3$ through the scattering of a delayed X-ray or ultraviolet attosecond probe pulse (frequency ω_3) off the AI packet consisting of two AI states with decay times τ_{r1} and τ_{r2} and frequency detunings $\Delta_k = \omega_k - \omega_g - (\omega_1 - \omega_2)$, where $k = 1, 2$. The intensity of the CARS signal is controlled here by four Fano parameters. Two of these parameters, q'_1 and q'_2 , quantify the pump- and Stokes-field-induced coupling of the first and second AI states, respectively, to the g state. The other two Fano parameters, q''_1 and q''_2 , characterize the coupling of the first and second AI states to the g state through the interaction with the probe and anti-Stokes fields (see Fig. 15). Measuring

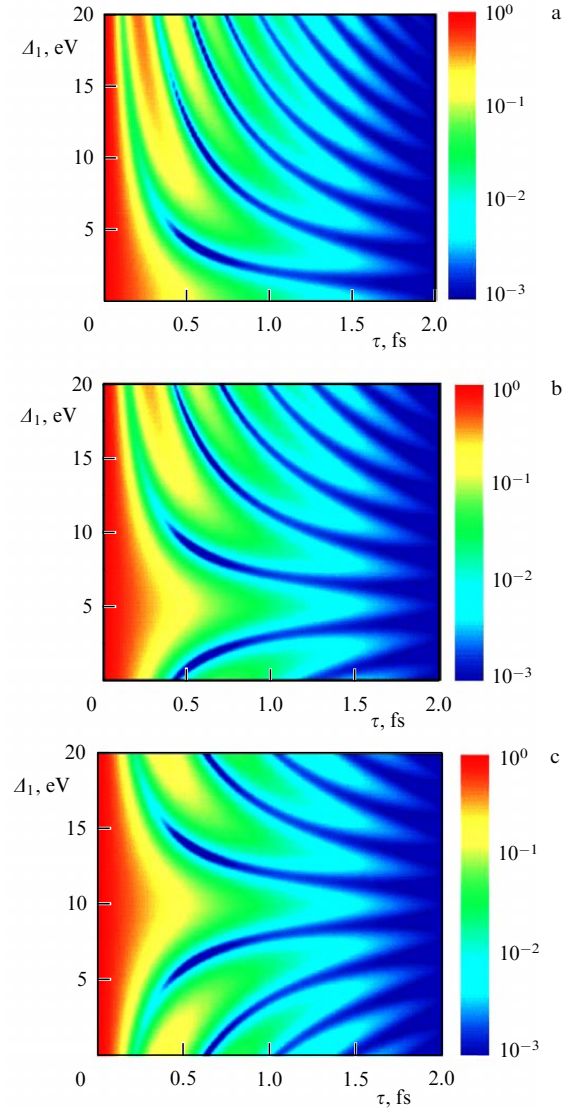


Figure 16. CARS spectrochronography of a packet of AI states: the intensity of the CARS signal as a function of the frequency detuning Δ_1 and delay time τ of the probe pulse relative to the pump and Stokes pulses for $\tau_{r1} = 0.8$ fs, $\tau_{r2} = 0.4$ fs, $q'_1 = q'_2 = q''_1 = q''_2 = 1$, $\Delta_2 = 0$ (a), 5 eV (b), and 10 eV (c).

the intensity of the frequency-resolved CARS signal as a function of the delay time τ between the probe pulse and the pump and Stokes pulses (attosecond CARS spectrochronography), one can separate the decay pathways of a many-electron system related to the interfering AI states, as well as find the decay times and parameters of coupling between the discrete and continuum states for each of the AI levels. Thus, CARS spectrochronography enables detection and analysis of autoionization phenomena in a fully optical format [161, 169], i.e., using only optical means for the excitation and probing of a quantum system, as well as for the detection of its response. For a broad class of physical systems and attosecond phenomena, a fully optical scheme of studies is not only convenient from the practical standpoint, but is also the only possible approach [170]. This is the case, in particular, in studies dealing with ultrafast electronic processes in the bulk of fluids and solids, where the methods based on the detection of charged particles become inapplicable.

14. Conclusion

Advances in laser technologies are opening new avenues in optical physics, giving access to physical phenomena on the femto- and attosecond time scales. Many of the experimental strategies of this rapidly developing field of research are based on Raman light scattering. In the regime of ultrashort pulses, Raman scattering gives rise to new effects, enabling a highly efficient frequency conversion of ultrashort light pulses and the synthesis of extremely short field waveforms within broad ranges of frequencies, field intensities, and pulse widths. Methods based on the Raman scattering of ultrashort laser pulses offer unique possibilities for the investigation of ultrafast processes on the femto- and attosecond time scales in a fully optical format, giving powerful momentum to the development of new approaches enabling a highly sensitive and highly selective microspectroscopy of physical, chemical, and biological systems.

Acknowledgments

I am pleased to gratefully acknowledge fruitful collaboration and illuminating discussions with A B Fedotov, D A Sidorov-Biryukov, A A Voronin, E E Serebryannikov, I V Fedotov, A D Savvin, A A Lanin, L V Doronina-Amitonova, Yu M Mikhailova, P A Zhokhov, V T Platonenko, and V P Mitrokhin (Physics Department, M V Lomonosov Moscow State University), A A Ivanov and M V Alfimov (Center of Photochemistry, Russian Academy of Sciences), A Baltuška and A-J Verhoef (Technological University of Vienna), E Goulielmakis, G Korn, and F Krausz (Max Planck Institute for Quantum Optics, Garching), V Ya Panchenko (Institute of Advanced Laser and Information Technologies, Russian Academy of Sciences), R Miles, M Shneider, and S Suckewer (Princeton University), A V Sokolov and M O Scully (Texas A&M University), M Yu Ivanov (Imperial College, London), Sunney Xie (Harvard University), K V Anokhin (P K Anokhin Institute of Normal Physiology, Russian Academy of Medical Sciences), Ching-yue Wang, Minglie Hu, and Yanfeng Li (Tianjin University), and M Motzkus (Heidelberg University).

References

- Raman C V, Krishnan K S *Nature* **121** 507 (1928)
- Raman C V, Krishnan K S *Nature* **121** 711 (1928)
- Raman C V, Krishnan K S *Nature* **122** 12 (1928)
- Raman C V *Nature* **123** 50 (1929)
- Landsberg G, Mandelstam L *Naturwissenschaften* **16** 557 (1928)
- Fabelinskii I L *Usp. Fiz. Nauk* **168** 1341 (1998) [*Phys. Usp.* **41** 1229 (1998)]
- Fabelinskii I L *Usp. Fiz. Nauk* **173** 1137 (2003) [*Phys. Usp.* **46** 1105 (1998)]
- Ginzburg V L, Fabelinskii I L *Vestn. Ross. Akad. Nauk* **73** 215 (2003) [*Herald Russ. Acad. Sci.* **73** 152 (2003)]
- Woodbury E J, Ng W K *Proc. IRE* **50** 2347 (1962)
- Bloembergen N *Nonlinear Optics* (New York: W.A. Benjamin, 1965)
- Maker P D, Terhune R W *Phys. Rev.* **137** A801 (1965)
- Shen Y R *The Principles of Nonlinear Optics* (New York: Wiley, 1984)
- Zheltikov A M *Sverkhkhorotkie Impul'sy i Metody Nelineinoi Optiki* (Ultrashort Pulses and Nonlinear Optics Methods) (Moscow: Fizmatlit, 2006)
- Agrawal G P *Nonlinear Fiber Optics* (San Diego: Academic Press, 2001)
- Schmitt M et al. *J. Phys. Chem. A* **102** 4059 (1998)
- Gräfe S et al. *J. Raman Spectrosc.* **38** 998 (2007)
- Sokolov A V et al. *Phys. Rev. Lett.* **85** 562 (2000)
- Zhavoronkov N, Korn G *Phys. Rev. Lett.* **88** 203901 (2002)
- Zheltikov A M *Usp. Fiz. Nauk* **172** 743 (2002) [*Phys. Usp.* **45** 687 (2002)]
- Druet S A J, Taran J-P E *Prog. Quantum Electron.* **7** 1 (1981)
- Akhmanov S A, Koroteev N I *Metody Nelineinoi Optiki v Spektroskopii Rasseyaniya Sveta: Aktivnaya Spektroskopiya Rasseyaniya Sveta* (Methods of Nonlinear Optics in Light Scattering Spectroscopy: Active Spectroscopy of Light Scattering) (Moscow: Nauka, 1981)
- Akhmanov S A, Koroteev N I *Usp. Fiz. Nauk* **123** 405 (1977) [*Sov. Phys. Usp.* **20** 899 (1977)]
- Koroteev N I *Usp. Fiz. Nauk* **152** 493 (1987) [*Sov. Phys. Usp.* **30** 628 (1987)]
- Zheltikov A M, Koroteev N I *Usp. Fiz. Nauk* **169** 385 (1999) [*Phys. Usp.* **42** 321 (1999)]
- Zheltikov A M *J. Raman Spectrosc.* **31** 653 (2000)
- Zumbusch A, Holtom G R, Xie X S *Phys. Rev. Lett.* **82** 4142 (1999)
- Evans C L et al. *Proc. Natl. Acad. Sci. USA* **102** 16807 (2005)
- Scully M O et al. *Proc. Natl. Acad. Sci. USA* **99** 10994 (2002)
- Kocharovskiy V et al. *Proc. Natl. Acad. Sci. USA* **102** 7806 (2005)
- Pestov D et al. *Science* **316** 265 (2007)
- Zheltikov A M, Shneider M N, Miles R B *Appl. Phys. B* **83** 149 (2006)
- Zheltikov A, L'Huillier A, Krausz F "Nonlinear optics", in *Springer Handbook of Lasers and Optics* (Ed. F Träger) (New York: Springer, 2007) p. 157
- Harris S E, Sokolov A V *Phys. Rev. Lett.* **81** 2894 (1998)
- Sokolov A V, Yavuz D D, Harris S E *Opt. Lett.* **24** 557 (1999)
- Nazarkin A et al. *Phys. Rev. Lett.* **83** 2560 (1999)
- Wittmann M, Nazarkin A, Korn G *Phys. Rev. Lett.* **84** 5508 (2000)
- Dianov E M et al. *Pis'ma Zh. Eksp. Teor. Fiz.* **41** 242 (1985) [*JETP Lett.* **41** 294 (1985)]
- Mitschke F M, Mollenauer L F *Opt. Lett.* **11** 659 (1986)
- Zheltikov A M *Usp. Fiz. Nauk* **176** 623 (2006) [*Phys. Usp.* **49** 605 (2006)]
- Zheltikov A M *Opt. Commun.* **282** 985 (2009)
- Oron D et al. *Phys. Rev. A* **65** 043408 (2002)
- Simon M et al. *Phys. Rev. A* **73** 020706(R) (2006)
- Reeves W H et al. *Nature* **424** 511 (2003)
- Konorov S O, Fedotov A B, Zheltikov A M *Opt. Lett.* **28** 1448 (2003)
- Akimov D A et al. *Appl. Phys. B* **76** 515 (2003)
- Zheltikov A M *Phys. Rev. A* **79** 023823 (2009)
- Blow K J, Wood D *IEEE J. Quantum Electron.* **25** 2665 (1989)
- Stolen R H et al. *J. Opt. Soc. Am. B* **6** 1159 (1989)
- Bergé L et al. *Rep. Prog. Phys.* **70** 1633 (2007)
- Couairon A, Mysyrowicz A *Phys. Rep.* **441** 47 (2007)
- Mlejnek M, Wright E M, Moloney J V *Opt. Lett.* **23** 382 (1998)
- Lin Q et al. *Opt. Express* **14** 4786 (2006)
- Gordon J P *Opt. Lett.* **11** 662 (1986)
- Santhanam J, Agrawal G P *Opt. Commun.* **222** 413 (2003)
- Lin C H et al. *Phys. Rev. A* **13** 813 (1976)
- Ripoche J-F et al. *Opt. Commun.* **135** 310 (1997)
- Nibbering E T J et al. *J. Opt. Soc. Am. B* **14** 650 (1997)
- Nitsch W, Kiefer W *Opt. Commun.* **23** 240 (1977)
- Stapelfeldt H, Seideman T *Rev. Mod. Phys.* **75** 543 (2003)
- Zheltikov A M *J. Raman Spectrosc.* **39** 756 (2008)
- Morgen M et al. *J. Chem. Phys.* **102** 8780 (1995)
- Fedotov I V, Savvin A D, Fedotov A B, Zheltikov A M *Opt. Lett.* **32** 1275 (2007)
- Zheltikov A M *Opt. Lett.* **32** 2052 (2007)
- Calegari F et al. *Phys. Rev. Lett.* **100** 123006 (2008)
- Zheltikov A M *Usp. Fiz. Nauk* **177** 737 (2007) [*Phys. Usp.* **50** 705 (2007)]
- Walrafen G E, Krishnan P N *Appl. Opt.* **21** 359 (1982)
- Hollenbeck D, Cantrell C D *J. Opt. Soc. Am. B* **19** 2886 (2002)
- Lines M E *J. Appl. Phys.* **62** 4363 (1987)
- Knight J C et al. *Opt. Lett.* **21** 1547 (1996)
- Cregan R F et al. *Science* **285** 1537 (1999)
- Smith C M et al. *Nature* **424** 657 (2003)
- Zheltikov A M *Usp. Fiz. Nauk* **174** 1301 (2004) [*Phys. Usp.* **47** 1205 (2004)]

73. Zheltikov A M *Optika Mikrostrukturirovannykh Volokon* (Optics of Microstructure Fibers) (Moscow: Nauka, 2004)
74. Zheltikov A M *Nature Mater.* **4** 267 (2005)
75. Russell P *Science* **299** 358 (2003)
76. Knight J C *Nature* **424** 847 (2003)
77. Zheltikov A M *Usp. Fiz. Nauk* **170** 1203 (2000) [*Phys. Usp.* **43** 1125 (2000)]
78. Russell P St J J. *Lightwave Technol.* **24** 4729 (2006)
79. Zheltikov A M *Mikrostrukturirovannyye Svetovody v Opticheskikh Tekhnologiyakh* (Microstructure Fibers in Optical Technologies) (Moscow: Fizmatlit, 2009)
80. Liu X et al. *Opt. Lett.* **26** 358 (2001)
81. Serebryannikov E E et al. *Phys. Rev. E* **72** 056603 (2005)
82. Paulsen H N et al. *Opt. Lett.* **28** 1123 (2003)
83. Konorov S O et al. *Phys. Rev. E* **70** 057601 (2004)
84. Sidorov-Biryukov D A, Serebryannikov E E, Zheltikov A M *Opt. Lett.* **31** 2323 (2006)
85. Ivanov A A, Podshivalov A A, Zheltikov A M *Opt. Lett.* **31** 3318 (2006)
86. Kano H, Hamaguchi H *Opt. Express* **13** 1322 (2005)
87. Andresen E R et al. *J. Opt. Soc. Am. B* **22** 1934 (2005)
88. von Vacano B, Wohlleben W, Motzkus M *Opt. Lett.* **31** 413 (2006)
89. Zheltikov A M *J. Raman Spectrosc.* **38** 1052 (2007)
90. Doronina L V et al. *Opt. Lett.* **34** 3373 (2009)
91. Ishii N et al. *Phys. Rev. E* **74** 036617 (2006)
92. Teisset C et al. *Opt. Express* **13** 6550 (2005)
93. Mamyshev P V, Chernikov S V *Opt. Lett.* **15** 1076 (1990)
94. Kibler B, Dudley J M, Coen S *Appl. Phys. B* **81** 337 (2005)
95. Zheltikov A M *Phys. Rev. E* **75** 037603 (2007)
96. Liu B-W et al. *Opt. Express* **16** 14987 (2008)
97. Akimov D A et al. *Opt. Lett.* **28** 1948 (2003)
98. Limpert J et al. *IEEE J. Selected Topics Quantum Electron.* **12** 233 (2006)
99. Liu B-W et al. *Laser Phys. Lett.* **6** 44 (2009)
100. Voronin A A, Zheltikov A M *Zh. Eksp. Teor. Fiz.* **133** 687 (2008) [*JETP* **106** 597 (2008)]
101. Song Y-J et al. *Laser Phys. Lett.* **7** 230 (2010)
102. Röser F et al. *Opt. Lett.* **32** 3495 (2007)
103. Südmeyer T et al. *Opt. Lett.* **28** 1951 (2003)
104. Schenkel B, Paschotta R, Keller U *J. Opt. Soc. Am. B* **22** 687 (2005)
105. Ouzounov D et al. *Opt. Express* **13** 6153 (2005)
106. Bessonov A D, Zheltikov A M *Phys. Rev. E* **73** 066618 (2006)
107. Serebryannikov E E, Zheltikov A M *Phys. Rev. A* **76** 013820 (2007)
108. Fedotov A B et al. *Opt. Lett.* **34** 851 (2009)
109. Foster M et al. *Opt. Express* **13** 6848 (2005)
110. Tognetti M V, Crespo H M *J. Opt. Soc. Am. B* **24** 1410 (2007)
111. Voronin A A, Zheltikov A M *Phys. Rev. A* **78** 063834 (2008)
112. Eidam T et al. *Appl. Phys. B* **92** 9 (2008)
113. Fedotov I V et al. *Kvantovaya Elektron.* **39** 634 (2009) [*Quantum Electron.* **39** 634 (2009)]
114. Fedotov I V et al., in *CLEO-Europe 2009: Conf. on Lasers and Electro-Optics, Munich, Germany, 14–19 June 2009*
115. Konorov S O et al. *Pis'ma Zh. Eksp. Teor. Fiz.* **81** 65 (2005) [*JETP Lett.* **81** 58 (2005)]
116. Skryabin D V et al. *Science* **301** 1705 (2003)
117. Biancalana F, Skryabin D V, Yulin A V *Phys. Rev. E* **70** 016615 (2004)
118. Herrmann J et al. *Phys. Rev. Lett.* **88** 173901 (2002)
119. Brabec T, Krausz F *Phys. Rev. Lett.* **78** 3282 (1997)
120. Paul P M et al. *Science* **292** 1689 (2001)
121. Drescher M et al. *Science* **291** 1923 (2001)
122. Corkum P B, Krausz F *Nature Phys.* **3** 381 (2007)
123. Krausz F, Ivanov M *Rev. Mod. Phys.* **81** 163 (2009)
124. Hentschel M et al. *Nature* **414** 509 (2001)
125. Drescher M et al. *Nature* **419** 803 (2002)
126. Niikura H et al. *Nature* **417** 917 (2002)
127. Niikura H, Villeneuve D M, Corkum P B *Phys. Rev. Lett.* **94** 083003 (2005)
128. Goulielmakis E et al. *Science* **305** 1267 (2004)
129. Kienberger R et al. *Science* **297** 1144 (2002)
130. Uiberacker M et al. *Nature* **446** 627 (2007)
131. Cavalieri A L et al. *Nature* **449** 1029 (2007)
132. Corkum P B *Phys. Rev. Lett.* **71** 1994 (1993)
133. Zheltikov A M et al., Preprint No. 5 (Moscow: Phys. Dept., Moscow State Univ., 1988)
134. Fedotov A B, Gladkov S M, Koroteev N I, Zheltikov A M *J. Opt. Soc. Am. B* **8** 363 (1991)
135. Goulielmakis E et al. *Science* **320** 1614 (2008)
136. Cheng W et al. *Phys. Rev. Lett.* **94** 045003 (2005)
137. Malkin V M, Fisch N J, Wurtele J S *Phys. Rev. E* **75** 026404 (2007)
138. Voronin A A, Fedotov I V, Fedotov A B, Zheltikov A M *Opt. Lett.* **34** 569 (2009)
139. Evans C L, Xie X S *Annu. Rev. Anal. Chem.* **1** 883 (2008)
140. Dudovich N, Oron D, Silberberg Y *Nature* **418** 512 (2002)
141. Dudovich N, Oron D, Silberberg Y *J. Chem. Phys.* **118** 9208 (2003)
142. Tai K et al. *Appl. Phys. Lett.* **49** 236 (1986)
143. Potasek M J, Agrawal G P *Phys. Rev. A* **36** 3862 (1987)
144. Agrawal G P *Phys. Rev. Lett.* **59** 880 (1987)
145. Serebryannikov E E et al. *Phys. Rev. E* **72** 027601 (2005)
146. Fedotov A B et al. *Opt. Commun.* **255** 218 (2005)
147. Chen J S et al. *Opt. Lett.* **31** 873 (2006)
148. Zheltikov A M *Pis'ma Zh. Eksp. Teor. Fiz.* **85** 667 (2007) [*JETP Lett.* **85** 539 (2007)]
149. Sabbah A J, Riffe D M *Phys. Rev. B* **66** 165217 (2002)
150. Siders C W et al. *Science* **286** 1340 (1999)
151. Hase M et al. *Nature* **426** 51 (2003)
152. Ishioka K et al. *Appl. Phys. Lett.* **89** 231916 (2006)
153. Zhi M, Wang X, Sokolov A V *Opt. Express* **16** 12139 (2008)
154. Savvin A D et al. *Opt. Lett.* **35** 919 (2010)
155. Oberthaler M, Höpfel R A *Appl. Phys. Lett.* **63** 1017 (1993)
156. Sidorov-Biryukov D A et al. *Opt. Express* **16** 2502 (2008)
157. Solin S A, Ramdas A K *Phys. Rev. B* **1** 1687 (1970)
158. Levenson M D, Flytzanis C, Bloembergen N *Phys. Rev. B* **6** 3962 (1972)
159. Gladkov S M et al. *Opt. Spektrosk.* **65** 249 (1988) [*Opt. Spectrosc.* **65** 149 (1988)]
160. Naumov A N et al. *Laser Phys.* **11** 1319 (2001)
161. Zheltikov A M et al. *Phys. Rev. Lett.* **103** 033901 (2009)
162. Wickenhauser M et al. *Phys. Rev. Lett.* **94** 023002 (2005)
163. Zheltikov A M, Ilyasov O S, Koroteev N I *Pis'ma Zh. Eksp. Teor. Fiz.* **54** 143 (1991) [*JETP Lett.* **54** 139 (1991)]
164. Fano U *Phys. Rev.* **124** 1866 (1961)
165. Armstrong J A, Wynne J J, in *Nonlinear Spectroscopy* (Ed. N Bloembergen) (Amsterdam: North-Holland, 1977) p. 152
166. Beutler H Z. *Phys.* **93** 177 (1935)
167. Armstrong J A, Wynne J J *Phys. Rev. Lett.* **33** 1183 (1974)
168. Armstrong L (Jr.), Beers B L *Phys. Rev. Lett.* **34** 1290 (1975)
169. Zheltikov A M *Phys. Rev. A* **74** 053403 (2006)
170. Verhoef A J et al. *Phys. Rev. Lett.* **104** 163904 (2010)